



## DEFENSE TECHNICAL INFORMATION CENTER

*Information for the Defense Community*

DTIC® has determined on 

Month	Day	Year
11	25	2008

 that this Technical Document has the Distribution Statement checked below. The current distribution for this document can be found in the DTIC® Technical Report Database.

- ☒ **DISTRIBUTION STATEMENT A.** Approved for public release; distribution is unlimited.
- ☐ **© COPYRIGHTED.** U.S. Government or Federal Rights License. All other rights and uses except those permitted by copyright law are reserved by the copyright owner.
- ☐ **DISTRIBUTION STATEMENT B.** Distribution authorized to U.S. Government agencies only. Other requests for this document shall be referred to controlling office.
- ☐ **DISTRIBUTION STATEMENT C.** Distribution authorized to U.S. Government Agencies and their contractors. Other requests for this document shall be referred to controlling office.
- ☐ **DISTRIBUTION STATEMENT D.** Distribution authorized to the Department of Defense and U.S. DoD contractors only. Other requests shall be referred to controlling office.
- ☐ **DISTRIBUTION STATEMENT E.** Distribution authorized to DoD Components only. Other requests shall be referred to controlling office.
- ☐ **DISTRIBUTION STATEMENT F.** Further dissemination only as directed by controlling office or higher DoD authority.
- Distribution Statement F is also used when a document does not contain a distribution statement and no distribution statement can be determined.*
- ☐ **DISTRIBUTION STATEMENT X.** Distribution authorized to U.S. Government Agencies and private individuals or enterprises eligible to obtain export-controlled technical data in accordance with DoDD 5230.25.

TNO Report

**TNO | Knowledge for business**



**20081124183**



Oude Waalsdorperweg 63  
P.O. Box 96864  
2509 JG The Hague  
The Netherlands

www.tno.nl

T +31 70 374 00 00

F +31 70 328 09 61

info-DenV@tno.nl

**TNO report**

**TNO-DV 2008 A176**

**The prospects of SAS interferometry for detection  
and classification**

Date	October 2008
Author(s)	Dr R. van Vossen B.A.J. Quesson Dr J.C. Sabel
Classification report	Ongerubriceerd
Classified by	LTZI B.E.A. Kerstens, MSc
Classification date	3 September 2008 (This classification will not change)
Title	Ongerubriceerd
Managementuitreksel	Ongerubriceerd
Abstract	Ongerubriceerd
Report text	Ongerubriceerd
Copy no	1
No. of copies	17
Number of pages	44 (excl. RIDP & distribution list)

The classification designation Ongerubriceerd is equivalent to Unclassified, Stg. Confidentieel is equivalent to Confidential and Stg. Geheim is equivalent to Secret.

All rights reserved. No part of this report may be reproduced in any form by print, photoprint, microfilm or any other means without the previous written permission from TNO.

All information which is classified according to Dutch regulations shall be treated by the recipient in the same way as classified information of corresponding value in his own country. No part of this information will be disclosed to any third party.

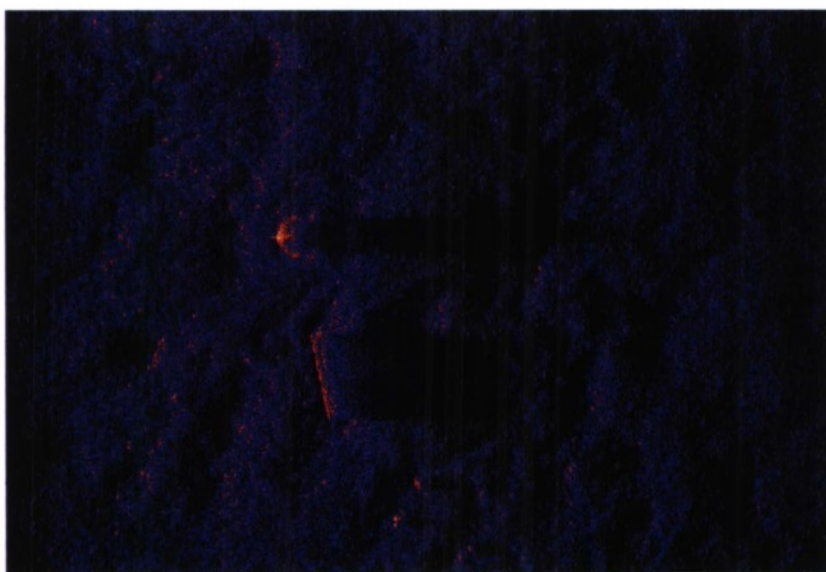
In case this report was drafted on instructions from the Ministry of Defence the rights and obligations of the principal and TNO are subject to the standard conditions for research and development instructions, established by the Ministry of Defence and TNO, if these conditions are declared applicable, or the relevant agreement concluded between the contracting parties.

© 2008 TNO

AQ F09-02-01022

# SAS interferometrie voor detectie en classificatie

Interferometrische SAS processing is ontwikkeld, getest en toegepast op data uit simulaties en uit een experiment met een sonar op een rail. De resultaten laten realistische hoogtes van de testobjecten zien. Als toepassing wordt detectie van begraven objecten beoogd, maar de methode is ook geschikt als hulpmiddel bij classificatie van bodemobjecten en voor bathymetrische survey.



## Probleemstelling

De akoestische detectie van in de zeebodem begraven objecten vormt een uitdaging, zelfs voor moderne sonarsystemen. Interferometrische synthetische apertuur sonar (inSAS) wordt gezien als een veelbelovende techniek om deze uitdaging het hoofd te bieden. Met behulp van inSAS kan onderscheid gemaakt worden tussen reflecties van verschillende hoogtes en wellicht kan de bodemecho onderdrukt worden ten gunste van echo's van begraven objecten. Zodoende kan naar verwachting de detectiekans verhoogd worden.

In het project Actieve SAS technologie is daarom gekozen voor het ontwikkelen en implementeren van inSAS. Het werk bouwt voort op de in voorgaande jaren ontwikkelde softwaresuite voor SAS processing, bewegingscorrectie en simulatie. Het rapport geeft de status van de ontwikkelingen weer als tussenrapportage.

Het project maakt deel uit van het doel-financieringsprogramma V512, Sonar en onderwater propagatie en de opdrachtgever is de Defensie Materieel Organisatie.

## Beschrijving van de werkzaamheden

Om interferometrie toe te passen zijn data benodigd van twee parallelle sonararrays op verschillende hoogte die dezelfde scène afbeelden. Uit faseverschillen tussen beide afbeeldingen kunnen hoogteverschillen in de scène worden afgeleid.

Interferometrische processing verloopt via de tussenstappen: migratie, de beeldvormende techniek die voor beide arrays een fase-consistent beeld moet opleveren; co-registratie, waarbij de afbeeldingen zo nauwkeurig mogelijk over elkaar heen worden gepast; interferogram berekenen, waarbij de afbeeldingen 'van elkaar afgetrokken' worden; faseherstel (*phase unwrapping*), waarbij fasesprongen van meer dan twee pi ongedaan gemaakt worden en ten slotte het berekenen van een 'hoogtekaart', waarbij de faseverschillen op basis van geometrische gegevens worden omgerekend naar hoogteverschillen. Voor elk van deze fasen is software ontwikkeld en beproefd. Hiervoor zijn zowel synthetische data uit simulaties gebruikt als experimentele data van metingen op een rail.

## Resultaten en conclusies

Het resultaat van het beschreven werk is een inSAS processing suite waarmee relatieve hoogtes in een sonarbeeld berekend kunnen worden. De berekeningen met



hoogfrequente data geven objecthoogtes die realistisch zijn. Deze resultaten geven vertrouwen in de processing. Op diverse punten is de processing nog voor verbetering vatbaar, bijvoorbeeld robuustheid in aanwezigheid van multipad-propagatie en faseconsistentie van de SAS-beelden. Ook de toepassing op laagfrequente data zal nog nader onderzocht worden.

### Toepasbaarheid

In het algemeen is de interferometrische processing ontwikkeld om hoogteverschil-

len op de bodem (bathymetrie) in kaart te brengen, met name de hoogte van gedetecteerde mijnen ten behoeve van verbeterde classificatie hiervan. Meer specifiek zal interferometrie toegepast gaan worden voor detectie en classificatie van begraven objecten, zoals explosieven. Op dit gebied zal een experiment uitgevoerd gaan worden voor het detecteren van in modder weggezakte explosieven, waarbij de in dit project ontwikkelde processing toegepast zal gaan worden.

PROGRAMMA	PROJECT
Programmabegeleider LTZ1 drs. R.P.A. Dekeling, DMO/OT	Projectbegeleider LTZ1 drs. R.P.A. Dekeling, DMO/OT
Programmaleider dr.ir. J.C. Sabel, BU1, Onderwater Technologie	Projectleider dr.ir. J.C. Sabel, BU1, Onderwater Technologie
Programmatitel Sonar en onderwater propagatie	Projecttitel Actieve SAS technologie
Programmanummer V512	Projectnummer 015.34736
Programmaplanning Start 01-01-2005 Gereed 31-12-2008	Projectplanning Start 01-01-2005 Gereed 31-12-2008
Frequentie van overleg Met de programma / project- begeleider werd diverse malen gesproken over de invulling en de voortgang van het onderzoek.	Projectteam dr. R. van Vossen, B.A.J. Quesson, dr.ir. J.C. Sabel

### Contact en rapportinformatie

Oude Waalsdorperweg 63  
Postbus 96864  
2509 JG Den Haag

T +31 70 374 00 00  
F +31 70 328 09 61

info-DenV@tno.nl

**TNO-rapportnummer**  
TNO-DV 2008 A176

**Opdrachtnummer**  
-

**Datum**  
october 2008

**Auteur(s)**  
dr. R. van Vossen  
B.A.J. Quesson  
dr.ir. J.C. Sabel

**Rubricering rapport**  
Ongerubriceerd

## Summary

This report presents an overview of the theory and implementation of interferometric SAS processing at TNO. The objective of the technique is mainly to provide a possible solution for the detection of buried targets in mine-hunting or harbour protection scenarios, by distinguishing between echoes from objects at different heights, such as the sea bottom surface and buried objects within that bottom. Other applications are survey, and measurement of bathymetry in general. In mine-hunting, height information from interferometry may improve the detection and classification of naval mines.

The processing steps in interferometry, required to derive the relative heights, are the following:

- Generate a phase-consistent (SAS-)image for each receive array. Not all SAS processing techniques are phase-preserving, so an adequate technique, including motion compensation / autofocus, should be selected.
- *Co-register* (align) the images, based on information about the geometry and on correlation. Geometry-based correction is usually applied to the whole image, whereas correlation based co-registration is often applied to patches of the image. The dimensions of these patches have to be chosen carefully.
- Calculate the *interferogram* by cross-correlation of the two images,
- Undo possible phase jumps due to two pi ambiguities to obtain absolute phases, also known as *phase unwrapping*. In many applications, depending on the height variations and geometry, this is not a crucial step. Many two-dimensional phase unwrapping methods exist, with differences in sensitivity to noise, robustness and calculation time.
- Calculate the *height map* using geometrical information to convert absolute phase differences to height differences.

For each of these steps, processing software has been developed and tested. Testing has been carried out for both synthetic data from simulations and measured data from a rail experiment.

Promising results have been achieved with the developed processing. Both for simulated and for measured data, correct object heights are found, supporting the validity of the processing. Remaining improvements lie mainly in motion compensation and multipath mitigation, which both are aimed at improving the phase consistency.

The interferometric processing can be used for bathymetric mapping and as an aid in target classification. The ultimate objective is to improve the detection and classification of buried mines, although this concept will have to be demonstrated.

# Contents

	<b>Managementuittreksel.....</b>	<b>2</b>
	<b>Summary .....</b>	<b>4</b>
<b>1</b>	<b>Introduction.....</b>	<b>6</b>
<b>2</b>	<b>Interferometry.....</b>	<b>8</b>
2.1	The concept of interferometry .....	8
2.2	Image co-registration .....	10
2.3	Extracting local phase information .....	11
2.4	Implementation .....	13
<b>3</b>	<b>Interferometric SAS processing: simulated examples.....</b>	<b>15</b>
3.1	SIMONA SAS Simulator.....	15
3.2	SAS Processing: Imaging using Stolt migration.....	16
3.3	Example I: tilted plane.....	18
3.4	Example II: top part of a sphere.....	20
<b>4</b>	<b>SAS interferometry applied to DERA/GESMA rail data .....</b>	<b>23</b>
4.1	Introduction to the DERA/GESMA rail datasets.....	23
4.2	Description of processing sequences .....	25
4.3	Results on DERA/GESMA rail data set 011004 (75 m range).....	32
4.4	DERA/GESMA rail data set 051003 (25 m range).....	37
<b>5</b>	<b>Conclusions and outlook .....</b>	<b>41</b>
<b>6</b>	<b>References.....</b>	<b>42</b>
<b>7</b>	<b>Signature.....</b>	<b>44</b>



# 1 Introduction

Interferometry is a technique that is widely applied in scientific measurements to measure small differences in height or length. Optical applications are well-established. In sonar, and also in radar (SAR, synthetic aperture radar), interferometry is mainly used to determine height differences in a scene under observation [1], [2]. SAR applications often use multiple passes of the radar platform to determine small changes with time in the surveyed area. These changes may, for instance, be due to various geophysical processes, such as volcanic activity or water pressure on dams. This is known as *repeat pass interferometry* and can be achieved with only one receive antenna. Other applications of radar interferometry exist, but these are outside the scope of this report. Owing to the similarities between radar and sonar, techniques from radar can often be applied to sonar as well.

Sonar applications of interferometry are currently mainly found in bathymetric surveys, where variations in sea bottom topography (bathymetry) are mapped using interferometric side scan sonar, based on single-beam processing. This type of interferometry requires at least two arrays, which are vertically separated by a fixed distance, referred to as the baseline. SAS interferometry is quite similar as it is also applied to data from two receive arrays. The difference is that this processing is applied to images rather than single beams. Height differences in the scene under observation result in small differences between the SAS-images from each array. Using information about the geometry, these differences can be translated to height relative to a plane of Reference [3], [4], [5], [6].

Current international developments in interferometric SAS are mainly aimed at improving mine warfare capabilities, where height provides additional information about detected targets that helps classification. In particular on autonomous platforms (AUV's: autonomous underwater vehicles) [7], [8], automatic classification is essential in achieving the desired level of autonomy. Hence, all available extra information on detected targets is useful. However, these are applications where high-frequency, high-resolution sonar is used for detection of proud mines. An important shortfall in mine warfare capabilities is still the detection of buried mines, which remain hidden in high frequency sonar images. Detection in sediment (sand, mud) requires lower frequencies (roughly between 5 and 30 kHz, depending on sediment type), but at these frequencies resolution is much worse as a consequence of smaller bandwidth. Low-frequency SAS can then be applied to improve along-track resolution and signal-to-noise-ratio (SNR). In a single SAS-image, no distinction can be made between objects at the bottom surface or below the surface. Interferometry then may provide the decisive information whether or not the detected object is buried (i.e. it has negative height).

Using the sea floor as the reference height, a further possibility is to try and suppress all scattering from the bottom interface, for example by subtracting one image from the other. If this can be properly achieved (depending on bottom bathymetry and resolution, among others), only signals from below or above the bottom will remain, thereby enhancing the echo from buried targets. This TNO-patented approach is known as the SUBDIRECT algorithm, which can be investigated once the interferometric processing is fully functional. To test this approach experimentally, 'conventional' interferometry has to be developed first.



In the TNO-project 'Active SAS Technology', the development of interferometric SAS (inSAS) has been started. The goal is to develop inSAS processing for the detection of buried targets, as explained above. This report presents the current status of the development. Chapter 2 contains an overview of the theoretical background and required processing steps in SAS interferometry. The implementation of the theory in software has been tested on two types of data, simulated and measured. Chapter 3 presents results obtained with simulated data; Chapter 4 the results with measured data. The measured data have been obtained from a rail experiment in 1999 by DERA (currently QinetiQ) and GESMA, from the UK and France, respectively. Both the experimental set-up and the results are presented in Chapter 4. The report concludes with Chapter 5, which gives a review of the results and an outlook to further developments.

## 2 Interferometry

### 2.1 The concept of interferometry

The objectives of SAS interferometry are to obtain information on the height of the seafloor and to improve the classification of objects by retrieving information on their height and –if possible– shape (the latter depending on target dimensions and orientation, scattering strength, etc.). Interferometry requires that data are acquired by at least two arrays (Figure 2.1). These are separated by the baseline vector  $\mathbf{B}$ . As shown in Figure 2.1, this recording geometry enables us to detect subtle time differences between arrivals on array 1 and array 2 that are caused by elevation differences.

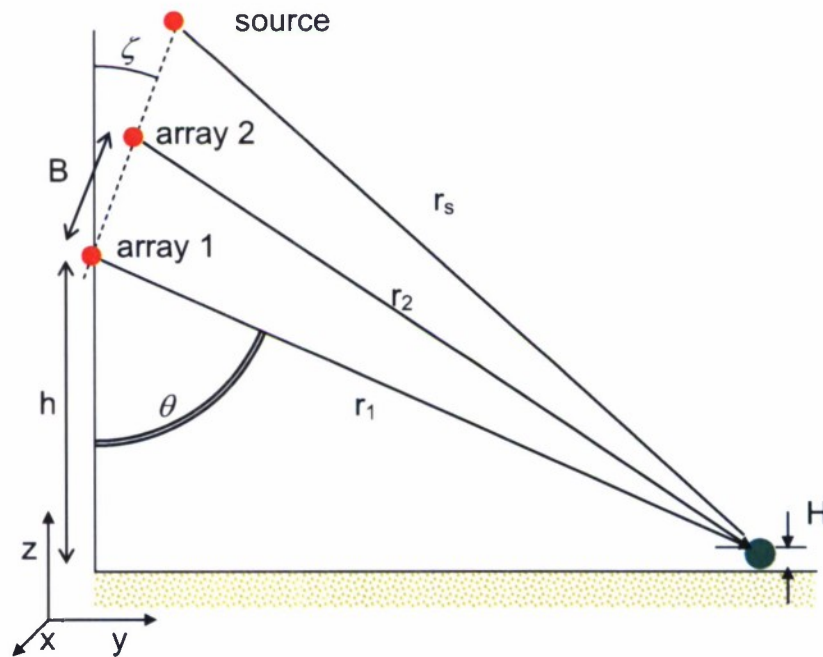


Figure 2.1 Configuration for SAS interferometry.

In the following, we assume that only one transmit element is used, i.e. phase differences only occur at the receiver side. We refer to the image constructed from the data acquired by array 1 as the master image; the image corresponding to array 2 is referred to as the slave image. Note that these images must be the result of processing that keeps the phases intact, so-called phase-preserving processing.

We denote the distance from the source to the target  $r_s$ , and  $r_1$  and  $r_2$  are the distances between the target and arrays 1 and 2, respectively. The two-way travel times, i.e. corresponding to the path from the source to the target and back to array 1 or 2, are denoted by  $t_{S1}$  and  $t_{S2}$ . These are:

$$t_{S1} = (r_s + r_1)c \quad t_{S2} = (r_s + r_2)c, \quad (2.1)$$

where  $c$  is the sound speed. In practical applications, the distance between the source and receivers is small compared to the distance to the target. The time axes are usually converted to the average distances  $r_{S1}$  and  $r_{S2}$ :

$$r_{S1} = \frac{r_S + r_1}{2} \quad r_{S2} = \frac{r_S + r_2}{2}, \quad (2.2)$$

such that the travel times can be easily converted to the average distances:

$$r_{S1} = \frac{t_{S1}}{2c} \quad r_{S2} = \frac{t_{S2}}{2c} \quad (2.3)$$

The quantities  $r_{S1}$  and  $r_{S2}$  are commonly referred to as the range axes in sonar images. Image display with respect to the range axis (instead of the two-way traveltime) facilitates the interpretation of sonar images.

We refer to the image constructed with the data recorded on array 1 as the master image, the image corresponding to array 2 is the slave image. In order to infer the height corresponding to the image pixel  $(x, r_{S1})$  in the master image, we have to find the corresponding image point in the slave image. If we succeed to determine the range difference between the corresponding pixels, we can infer the height of the pixel with a geometrical relationship. It should be explicitly stated that in the scenario under consideration, path differences only occur at the detector side. As a consequence, there is a factor of 2 difference between the one-way range difference  $r_2 - r_1$  and the two-way average range difference  $r_{S2} - r_{S1}$ .

Given the range difference, we obtain the height as follows (see Figure 2.1). First, we estimate the look angle  $\theta$  using

$$\cos(\theta + \zeta) = \frac{r_2^2 - B^2 - r_1^2}{2r_1 B}. \quad (2.4)$$

In this expression,  $\zeta$  is the angle of the baseline vector with the vertical axis (tilt angle). Then, the height  $H$  of the object relative to a reference height  $z = 0$ , e.g. the seafloor, is given by (see also Figure 2.1):

$$H(r_1) = h - r_1 \cos \theta \quad (2.5)$$

Thus, given the range shift between corresponding points in the master and the slave image, we can determine the height.

To find corresponding points in the master and slave images, first a *co-registration* is carried out. This step uses geometric information to relate events detected by array 1 to those detected by array 2. After this step, only the information that was not known a priori remains to be retrieved. This task is easier than retrieving all information from the data, i.e. retrieving already known information plus the new, yet unknown information. This step is carried out in step two by estimation of the *instantaneous phase difference*.

Hence, a two-step procedure is used to determine the range shift:

- 1 Image co-registration;
- 2 Estimating instantaneous phase differences.

In the image co-registration step, a range shift (which may vary with range) is determined using information about the geometry. The instantaneous phase information is then used to refine the resolution of the height information, i.e. to obtain local information on the shape of objects or on the bathymetry.

## 2.2 Image co-registration

In the co-registration step, we use information about the geometry to overlay the master and slave images. This is achieved by computing and applying a correction to the slave image such that  $r_1 = r_2$  with respect to the reference plane, the seafloor (see Figure 2.2). In this case we assume that the seafloor is (more or less) horizontal and that we know the measurement configuration, i.e. the height  $h$  of array 1 above the seafloor, the baseline  $B$ , and the tilt angle  $\zeta$  are known (Figure 2.2). In that case, we can estimate for each range  $r_1$  the corresponding range  $r_2$  using

$$r_2 = \sqrt{r_1^2 + B^2 + 2r_1 B \cos(\theta_c(r_1) + \zeta)}, \quad (2.6)$$

With  $\theta_c(r_1)$  the co-registration look angle corresponding to the direct path from array 1 to the seafloor. The co-registration look angle  $\theta_c(r_1)$  is calculated from:

$$\theta_c(r_1) = \cos^{-1}[h/r_1] \quad (2.7)$$

Geometry-based co-registration thus requires information about the acquisition geometry and a rough estimate of the bathymetry. When this information is not available or not reliable, data-driven (correlation-based) co-registration methods can be considered. These have been thoroughly investigated by [1] and [9].

When  $r_2$  is known, we can determine the one-way co-registration range shift  $\Delta r_c$ :

$$\Delta r_c = r_2 - r_1. \quad (2.8)$$

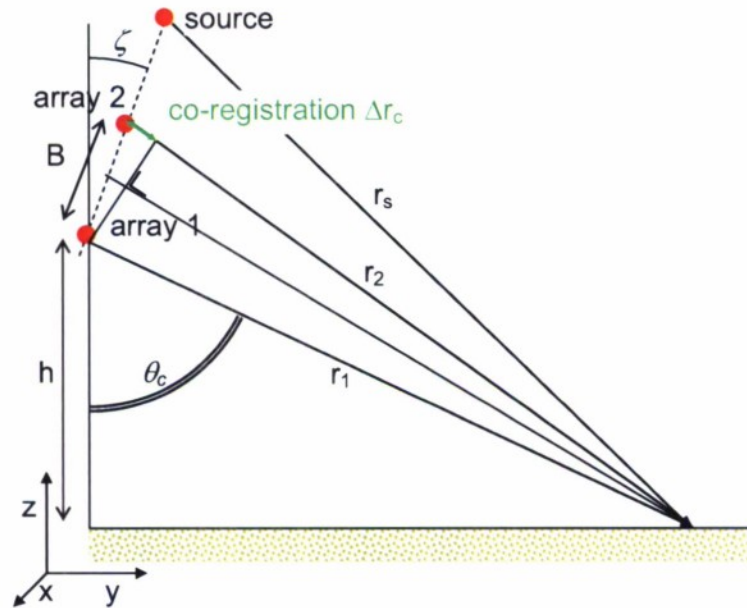


Figure 2.2 Configuration for SAS interferometry (co-registration).



### Implementation

The co-registration procedure comprises two steps:

- Compute and apply the co-registration range correction  $\Delta r_c(r_1)$  to the slave image, i.e. the range axis (average two-way distance) of the co-registered slave image becomes:  $r_{S2} \rightarrow r_{S2} - \frac{\Delta r_c(r_1)}{2}$ .
- Since this range shift generally differs from the range sampling, the master and slave images sample the range axis (average two-way distance) at different points. We denote the difference between these samples by  $\delta_r(r_{S1})$ . The sampling term yields a one-way range shift

$$\Delta r_s(r_{S1}) = 2\delta_r(r_{S1}) \quad (2.9)$$

We need to take this term into account since we did not resample the range axis (i.e. sampling the range axis at identical points as the master image) after the co-registration range correction. This resampling would require interpolation starting from a non-uniformly sampled range axis, and preserving the instantaneous phase in this interpolation procedure might be an issue.

- The total one-way range difference between two corresponding pixels contains a contribution of three terms, the co-registration, sampling (both determined from the co-registration), and the range difference derived from the instantaneous phase:

$$\Delta r_{tot} = \Delta r_c + \Delta r_s + \Delta r_i \quad (2.10)$$

In the next section we discuss the instantaneous phase contribution  $\Delta r_i$ .

## 2.3 Extracting local phase information

Image co-registration generally has a low resolution. This second step uses local phase information extracted from the master and slave images to gain resolution in the height map. This step is thus crucial for getting information on the shape of objects or on details of the bathymetry. The analysis of *complex trace attributes* enables us to retrieve this local phase information [10]. This can be measured using the instantaneous phase.

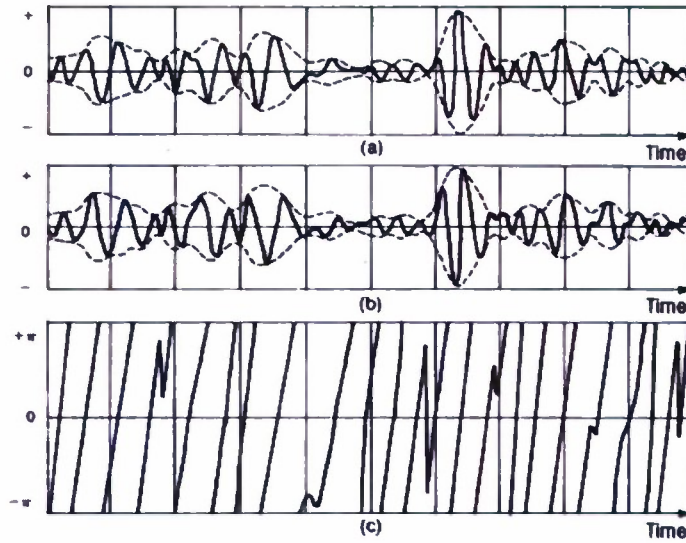


Figure 2.3 Complex-trace analysis. Real (a) and quadrature (b) traces for a portion of a trace. The envelope is shown as the dashed line in (a) and (b). Instantaneous phase is plotted in (c), reprinted from [11].

Figure 2.3 illustrates complex trace analysis. It shows a real and the corresponding quadrature trace (which can be obtained using the Hilbert transform), which we denote with  $h_r(t)$  and  $h_i(t)$ , respectively. The complex trace  $h(t)$  is then

$$h(t) = h_r(t) + j \cdot h_i(t), \quad (2.11)$$

where  $j$  denotes the complex unit vector. The envelope is defined as the amplitude of  $h(t)$ , the instantaneous phase is given by the phase angle of  $h(t)$ . In the following, we use the term phase information for the instantaneous phase. For band limited signals, the phase, or the phase difference  $\Delta\phi$  can be related to the travel time difference  $\Delta\tau = t - t_0$  according to:

$$\Delta\phi = 2\pi f_i \Delta\tau, \quad (2.12)$$

Where  $f_i$  is the instantaneous frequency [10]. We estimate the time differences and assign these to the centre frequency  $f_c$ . We further assume that the centre frequency  $f_c = f_i$ . Then, the instantaneous phase difference corresponds to the range difference

$$\Delta r_i = \frac{c \Delta\phi}{2\pi f_c}. \quad (2.13)$$

As illustrated in Figure 2.4, instantaneous phase gives only accurate time or range differences for narrowband data (and for small time shifts). Figure 2.4 shows that for a broadband LFM pulse ( $f_c = 150$  kHz,  $b = 60$  kHz), the error is 30% in the estimated time differences. Therefore, it is worthwhile to consider data analysis in different frequency bands. As an alternative, correlation methods can be used. The discontinuous jumps in the curves are a result of cycle skips. Figure 2.4 also illustrates the importance of the image co-registration. Instantaneous phase estimates are more accurate for small time differences. Finally, the right-hand graph shows that this type of error is not an issue for radar interferometry, because the relative bandwidth is usually much smaller.

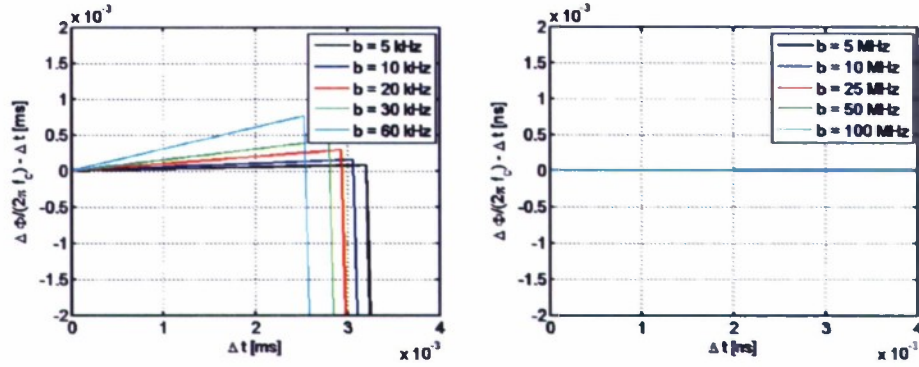


Figure 2.4 Difference between the 'true time shift'  $\Delta t$  and the time shift derived from the instantaneous phase as a function of the time shift for matched filtered LFM pulses with 150 kHz centre frequency and different bandwidths. The right graph shows this sensitivity analysis for a radar scenario with a 15 GHz centre frequency.

## 2.4 Implementation

We denote the co-registered images by  $U_1(m,n)$  and  $U_2(m,n)$ , where the indices  $m = 1, \dots, n_r$  and  $n = 1, \dots, n_x$  denote the samples of the range and azimuth axis, respectively. Both  $U_1(m,n)$  and  $U_2(m,n)$  are complex. Interferometry uses the differences in the instantaneous phase to obtain information on the height of the imaged area. The procedure consists of the following steps:

- Measure phase difference and construct the interferogram;  
We first define the correlation map  $C(m,n)$ :

$$C(m,n) = \frac{\sum_{p=-k}^k \sum_{q=-l}^l U_1(m+p, n+q) U_2^*(m+p, n+q)}{\left( \sum_{p=-k}^k \sum_{q=-l}^l |U_1(m+p, n+q)|^2 \right)^{1/2} \left( \sum_{p=-k}^k \sum_{q=-l}^l |U_2(m+p, n+q)|^2 \right)^{1/2}} \quad (2.14)$$

The correlation map is computed averaging over patches with a size of  $2k+1$  times  $2l+1$  elements. The amplitude of  $C(m,n)$  is considered to be an important measure of data quality [13], and is often used for creating a mask. Nevertheless, this measure is rather sensitive to *phase differences* between the master and slave images. Therefore, we use the correlation map of the instantaneous amplitudes as a measure for data quality instead.

The instantaneous phase of  $C(m,n)$  yields the phase difference between the master and slave images corresponding to image pixel  $(m,n)$ . The 2-D moving average (summation of neighbouring pixels) is applied to improve the signal-to-noise-ratio (SNR) of the phase estimate. Note that filtering of the correlation map is preferred over filtering of the phase values only [13].

- Apply phase unwrapping;  
Phase unwrapping is required since the instantaneous phase is bounded between  $-\pi$  and  $\pi$  (see Figure 2.3). As a result, ambiguity exists in the phase values, since a multiple factor of  $2\pi$  is left undetermined. Many algorithms exist to unwrap the phase. These algorithms are based on minimizing discontinuities in the data,

minimizing the length of branch cuts, and least squares algorithms. For a review of phase unwrapping methods, we refer to [13]. In our current implementation, we use the classical branch-cut (Goldstein) algorithm [12], [13]. 2-D phase unwrapping is an active field of research. For further development it would be worthwhile to investigate also so-called '*network approaches*' and '*synthesis algorithms*' [14], [15], [16].

- Estimate the height;

First estimate the range difference  $\Delta r_{tot}$  using Equation 2.10, then determine  $r_2$ :

$$r_2 = r_1 + \Delta r_{tot}. \quad (2.15)$$

The value of  $r_2$  is now used to compute the angle according to Equation 2.4, after which the height can be obtained using Equation 2.5.



### 3 Interferometric SAS processing: simulated examples

We proceed by illustrating SAS interferometry with simulated examples. Before discussing the examples, we first review the essential features for the simulation and processing [17], and analyse whether the phase information is preserved.

#### 3.1 SIMONA SAS Simulator

In this section we briefly review the main functionality of the SIMONA simulator. Let  $\mathbf{x}_r$  and  $\mathbf{x}_s$  denote the receiver and source positions and  $s(t)$  the source signal, respectively. The simulator models the wavefield  $U(t, \mathbf{x}_r; \mathbf{x}_s)$  scattered by a set of  $N$  point scatterers. It is given by:

$$U(\mathbf{x}_r; \mathbf{x}_s, t) = s(t) * \sum_{i=1}^N A_i(\mathbf{x}_r; \mathbf{x}_s) \delta(t - \tau_i(\mathbf{x}_r; \mathbf{x}_s)). \quad (3.1)$$

For each point scatterer, the response is obtained by convolving (\*) the source signature with the target response. It is characterized by a time delay  $\tau(\mathbf{x}_r; \mathbf{x}_s)$  and an amplitude response  $A(\mathbf{x}_r; \mathbf{x}_s)$ . The time delay is the propagation time from the source to the target and back to the receiver. The amplitude term includes both target strength and propagation loss.

Equation 3.1 is evaluated at discrete samples  $t = k\Delta t$ :

$$U(\mathbf{x}_r; \mathbf{x}_s, k\Delta t) = s(k\Delta t) * \sum_{i=1}^N A_i(\mathbf{x}_r; \mathbf{x}_s) \delta(k\Delta t - \tau_i(\mathbf{x}_r; \mathbf{x}_s)) \quad (3.2)$$

Since the time delays  $\tau_i(\mathbf{x}_r; \mathbf{x}_s)$  do not necessarily coincide with the discrete time samples  $k\Delta t$ , the wavefield obtained with Equation 3.2 does not guarantee that the phase information is correctly represented in  $U(\mathbf{x}_r; \mathbf{x}_s, k\Delta t)$ . Recall that phase errors can be substantial when the wavefield is sampled according to the Shannon sampling criterion (at least two samples are required per minimum wavelength).

In order to preserve the phase information, we evaluate the response of the scattered field in the frequency domain. Defining the Fourier transform (FT) as

$$f(\omega) = \int_{-\infty}^{\infty} f(t) \exp[-i\omega t] dt \quad (3.3)$$

with inverse transform (IFT)

$$f(t) = \frac{1}{2\pi} \int_{-\infty}^{\infty} f(\omega) \exp[i\omega t] d\omega, \quad (3.4)$$

Equation 3.2 can be written as:

$$U(\mathbf{x}_r; \mathbf{x}_s, k\Delta t) = IFT \left[ s(k\Delta\omega) \sum_{i=1}^N A_i(\mathbf{x}_r; \mathbf{x}_s) \exp[-ik\Delta\omega\tau_i(\mathbf{x}_r; \mathbf{x}_s)] \right]. \quad (3.5)$$

In this equation, the exact values for the time delays are used. As a result, phase information is correctly captured in  $U(\mathbf{x}_r; \mathbf{x}_s, k\Delta t)$ . The implementation for target strength is identical to the existing SAS Simulator (SIMONA [17]).

At this point it has to be stated that the existing SAS simulator (SIMONA [17]) did not capture the phase information correctly. Phase errors (on the order of  $\lambda/32$ ) were introduced in a procedure to optimise SIMONA for speed. It has been verified that these phase errors do not influence the SAS imaging. The reason is that these images display the instantaneous amplitude. As shown in Figure 2.3, the instantaneous amplitude varies smoothly in comparison to the instantaneous phase, and is therefore not sensitive to small phase errors. Interferometry, on the other hand, is based on the interpretation of subtle phase differences, and these phase differences may therefore be significant to interferometry [3]. The phase errors introduced (rounding errors) differ for each point scatterer and also for each array element.

For the development of interferometry, we used the frequency-domain implementation described in this section. This procedure guarantees that the phase information is correctly captured in the simulated data.

#### *Software*

The SAS simulator (Sourceforge → Source Code → SAS\_Simulator ) has the following structure:

- `create_input\main_input_sassimulator.m`: this code enables the user to specify the input to the SAS simulation and saves these settings in a parameter file. In the examples presented here, different targets have been used, and these are referred to with a character string, e.g. `id = 'test10'`; `create_input\define_target_test10.m`.
- `simulator\main_simulator.m` computes the pingfiles for the specified input and saves these in a directory `output_timetag (yyyymmddhhmm)`.

In the following, we refer to the simulation results using the character string `id`.

### 3.2 SAS Processing: Imaging using Stolt migration

Imaging or migration is the procedure that converts the zero-offset (phase centre) section of the measured data into an image of the medium. The following procedure assumes that the zero-offset section is a uniform linear array, and we denote the midpoint coordinate  $x$ . This coordinate is the average of the source and receive element positions.

As in the papers describing the Stolt migration [17], [18], we distinguish the recorded data from the migrated data introducing the arguments  $U(r = 0, x, t)$  to denote the recorded data and  $U(r, x, t = 0)$  for the imaged data, respectively. The recorded data are acquired at location  $x$  in the form of time series, and migration converts these time series into an image of the medium itself. This is represented by the scattering strength as a function of location  $(r, x)$ , where  $r$  indicates the range. The migration procedure converts hyperbolas to point scatterers corresponding to the correct image positions.

For underwater imaging, the migration can be efficiently implemented using Stolt migration [17], [18], [19]. This method assumes that the sound velocity in the medium is constant, which may lead to some defocusing in case of propagation through sediment (for buried objects). For now, we assume that this defocusing effect is

negligible, since we mainly consider shallowly buried objects and steep incidence angles. Additionally, the implementation requires a uniform linear data array. Stolt migration evaluates  $U(r, x, t = 0)$  in the frequency-wavenumber domain:

$$U(r, x, 0) = \frac{1}{2\pi} \int_{-\infty}^{\infty} d\omega \int_{-\infty}^{\infty} dk_x U(0, k_x, \omega) \exp \left[ i \left( \sqrt{\frac{4\omega^2}{c^2} - k_x^2} r + k_x x \right) \right], \quad (3.6)$$

where  $U(0, k_x, \omega)$  is obtained by taking the Fourier transform of the measured data  $U(0, x, t)$ ,

$$U(0, k_x, \omega) = \frac{1}{2\pi} \int_{-\infty}^{\infty} dt \int_{-\omega/c}^{\omega/c} dx U(0, x, t) \exp[-i(\omega t + k_x x)] \quad (3.7)$$

Stolt migration is based on the change of variables from the angular frequency  $\omega$  to the wavenumber  $k_r$  according to the formula:

$$k_r = \sqrt{\frac{4\omega^2}{c^2} - k_x^2}; \quad \omega = \frac{c}{2} \sqrt{k_x^2 + k_r^2}. \quad (3.8)$$

In order to compute Equation 3.6, we apply the coordinate transform and change the integration variable:

$$U(r, x, 0) = \frac{1}{2\pi} \int_{-\infty}^{\infty} dk_r \int_{-\omega/c}^{\omega/c} dk_x \left[ \frac{c}{2} \frac{k_r}{\sqrt{k_x^2 + k_r^2}} \right] U(k_r(\omega), k_x, 0) \exp[i(k_r r + k_x x)]. \quad (3.9)$$

The evaluation of the Fourier transform (with respect to  $k_r$ ) requires that the wavenumber is discretised using equal spacing. This implies that we need  $U(0, k_x, \omega)$  at non-equally spaced locations which are obtained from Equation 3.8. These values are obtained by interpolation (spline).

#### Implementation

- 2-D Fourier transform of recorded data.
- Apply phase shift to account for time window  $t_0$ : multiply  $U(0, k_x, \omega)$  with  $\exp[i\omega t_0]$ ;  
Shifting property:  $\text{FT}(f(t)) \leftrightarrow f(\omega)$ ;  $\text{FT}(f(t + t_0)) \leftrightarrow f(\omega) \exp[i\omega t_0]$   
Input to Fourier transform:  $f(t - t_0)$ , which corresponds to multiplying with  $\exp[-i\omega t_0]$  in the frequency domain.
- Multiply now with  $\exp[ik_r r_0]$ , where  $k_r$  is given in Equation 3.8. This step has to be taken before the interpolation, and define the corresponding range axis.
- Prepare for inverse Fourier transform: variable substitution and computation of amplitude term (Jacobian).
- Interpolation to get  $U(k_r(\omega), k_x, 0)$  uniformly sampled. Approach: Define a linear array for  $k_r$  and compute the corresponding frequency values using Equation 3.8. Repeat this step for each value of the horizontal wavenumber. Use spline interpolation to obtain  $U(k_r(\omega), k_x, 0)$ .
- 2-D Inverse Fourier transform.

### Software

The SAS processor (Sourceforge → Source Code → SAS\_Processor) is organised as follows:

- The folder **dataQC** contains scripts for data visualisation and quality control.
- The folder **dataIO** contains scripts for data input-output.
- The **preprocessing** script (i.e. `create_sasinput_DERAGESMA_raildata_051003.m`) constructs the synthetic array from the individual ping files. The synthetic array is a uniform linear array. Motion compensation is an essential step in the preprocessing procedure.
- The folder **imaging** contains the migration/imaging codes (i.e. `create_sasoutput_simulations.m`).

## 3.3 Example I: tilted plane<sup>1</sup>

The first simulated example concerns a tilted plane, as illustrated in a 2D and a 3D view in Figure 3.1. The target is built up from individual point scatterers that are separated by  $\lambda/5 = 3.0$  mm. The target roughness is also 3.0 mm. The simulation parameters are listed in Table 3.1.

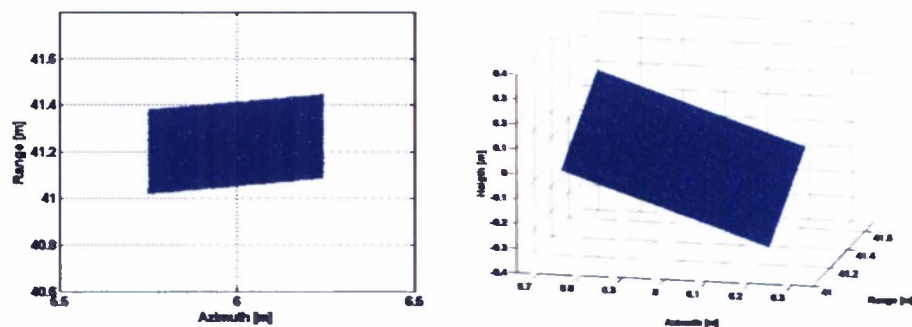


Figure 3.1 Top view (left) and 3-D view (right) of the tilted plane.

Table 3.1 Simulation parameters for the tilted plane example.

Pulse centre frequency $f_c$	100 kHz
Pulse bandwidth $b$	40 kHz
Pulse type	Linear frequency modulated pulse (LFM)
Pulse duration	6.4 ms
Length of synthetic aperture	12 m (from 0.0 to 12.0 m)
Number of pings	200
Number of elements/ping	8
Separation of elements	0.015 m
Displacement between pings	0.060 m
Platform height	10.0 m
Platform y-distance to target	40.0 m
Number of receive arrays	2
Baseline vector <b>B</b> (vertical separation)	(0, 0, 0.20) m
Source position	Centre of array 1

<sup>1</sup> Simulations, processing and interferometry: Software id = 'test10\_20080128'.



Having simulated the data, we apply Stolt migration to convert the SAS data to the image of the reflectivity of the tilted plane (Figure 3.2). Note that we did not include a background in the simulation.

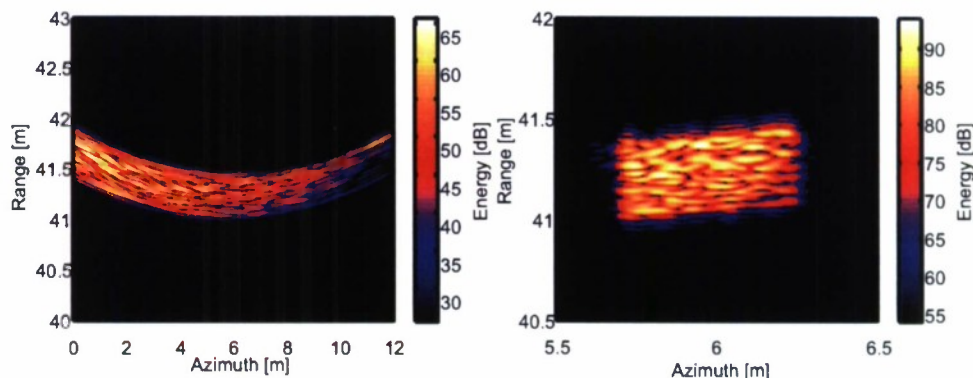


Figure 3.2 Simulated synthetic aperture sonar data (left) and migrated data (right) of the tilted plane illustrated in Figure 3.1. No background noise was simulated.

Subsequently, the height map is derived using interferometric processing:

- images are constructed using the data measured on both arrays;
- geometry-based co-registration is applied with respect to  $z = 0$ ;
- instantaneous phase differences are estimated;
- 2-D phase unwrapping;
- height estimation.

Figure 3.3 shows details of the SAS images derived from both arrays. The range shift induced by the baseline is approximately 0.02 m. The geometry-based co-registration compensates for this range shift. Similar to the configurations shown in Figure 2.1 and Figure 2.2, array 1 is the lower, array 2 the upper of the two. Therefore,  $r_2 > r_1$ , which explains the 0.02 m shift in range between the left and the centre panel of Figure 3.3.

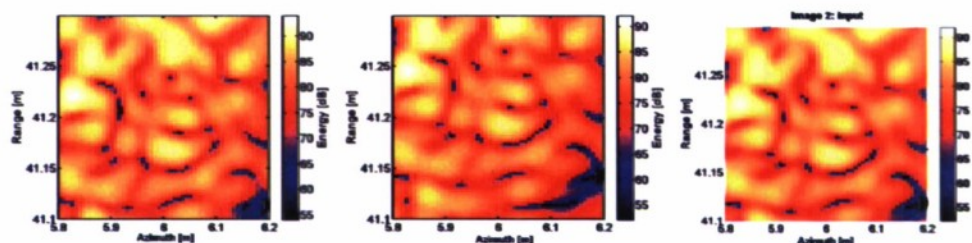


Figure 3.3 Detail of SAS images constructed from the lower array 1 (left panel) and the upper array 2 (centre panel). The geometrical range displacement between the images is approximately 0.02 m. The right panel shows the co-registered slave image.

Figure 3.4 displays the height estimated using the interferometric processing. For image pixels with a low scattering strength ( $-40$  dB relative to the maximum value), we set the height to  $z = 0$  (the phase information is then unreliable). A comparison of the interferometric height estimate to the shape of the 3-D target (Figure 3.1) shows a good agreement. This is confirmed by the 3-D reflectivity image (Figure 3.5). This image displays the reflectivity as a function of azimuth, range, and height.

The noise on the height estimates is a concern. Figure 3.5 shows that the peaks and valleys in the height estimates generally have a low reflectivity strength. This indicates

that sidelobes from strong scatterers (highlights) might influence the phase information. This results in unreliable phase information since it is not related to the corresponding image position in such a situation. Similar reasoning applies to the height estimates for locations outside the target.

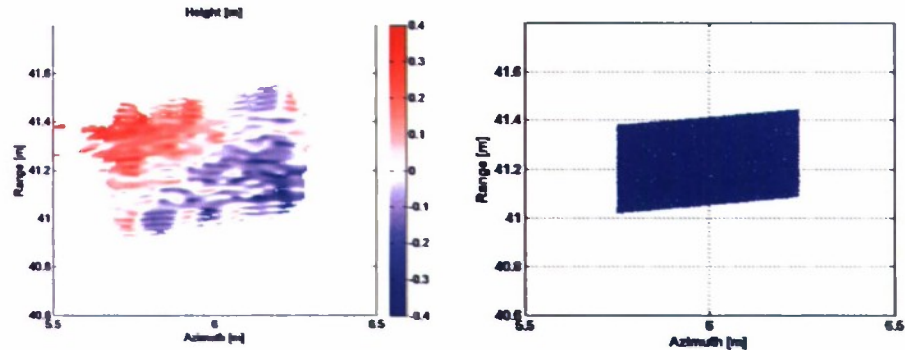


Figure 3.4 Interferometric height estimate (left) and target (right).

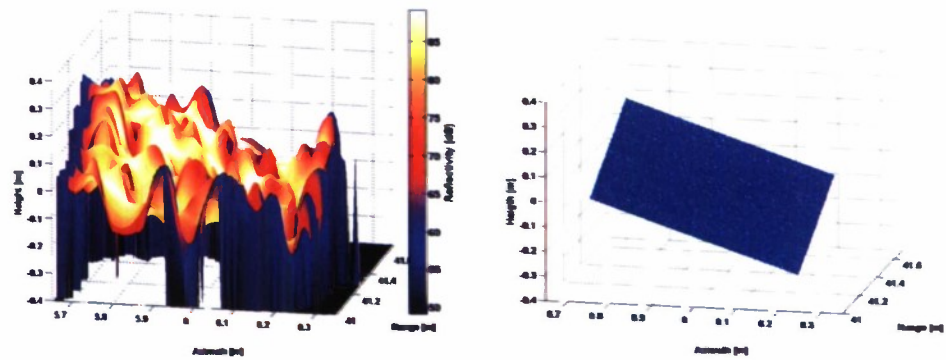


Figure 3.5 3-D view of reflectivity (left) and 3-D target (right). Note that the peaks and valleys in the reflectivity image have a low reflectivity strength.

### 3.4 Example II: top part of a sphere<sup>2</sup>

In the second simulated example we consider the top part of a sphere as a target. The centre of the hemispherical target is located at  $(x, y, z) = (6, 40, 0)$  m, see also Figure 3.9, right panel. The radius of the full sphere is 0.35 m. The other simulation parameters are identical to the previous example (Table 3.1).

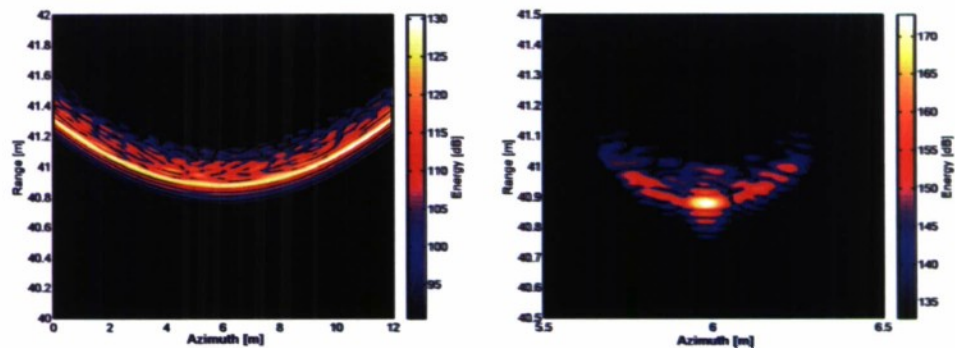


Figure 3.6 Simulated synthetic aperture sonar input data (left) and migrated data (right) for array 1.

<sup>2</sup> Simulations, processing and interferometry: Software id = 'test7\_20080128'.

Figure 3.6 shows the SAS input data and the corresponding image for array 1. Characteristic in images of a sphere is the strong highlight induced by normally incident waves; the target back-scattering strength is large for waves arriving at normal incidence. Diffuse scattering is determined by target roughness at different angles of incidence, and is therefore significantly smaller.

Figure 3.7 shows details of the SAS images derived from both arrays. The range shift induced by the baseline is, similar to the previous example, approximately 0.02 m. The geometry-based co-registration (with reference level  $z = 0$ ) compensates for this range shift. Note that sidelobes occur in the range direction due to the high amplitude signal.

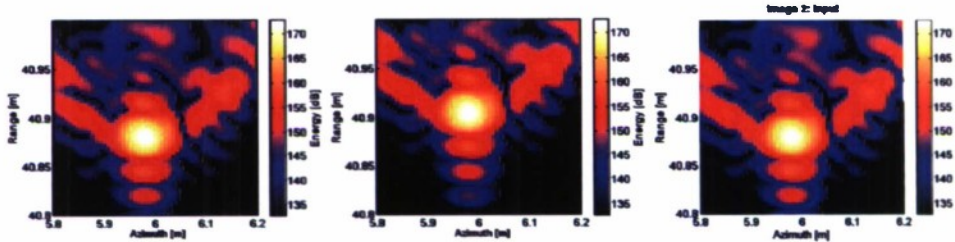


Figure 3.7 Detail of SAS images constructed from the lower array 1 (left panel) and the upper array 2 (centre panel). The geometrical range displacement between the images is approximately 0.02 m. The right panel shows the co-registered slave image.

Figure 3.8 shows the height inferred from interferometry. For image pixels with a low scattering strength ( $-40$  dB relative to the maximum value), we set the height to zero.

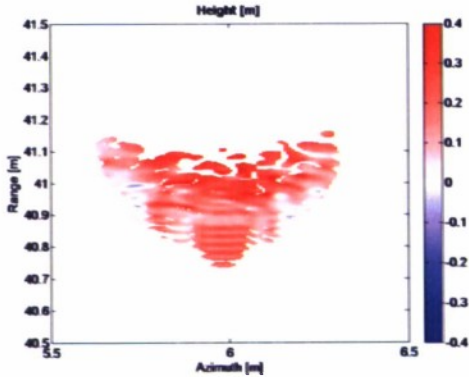


Figure 3.8 Interferometric height estimate for the hemispherical target. Note that the radius is 0.35 m.

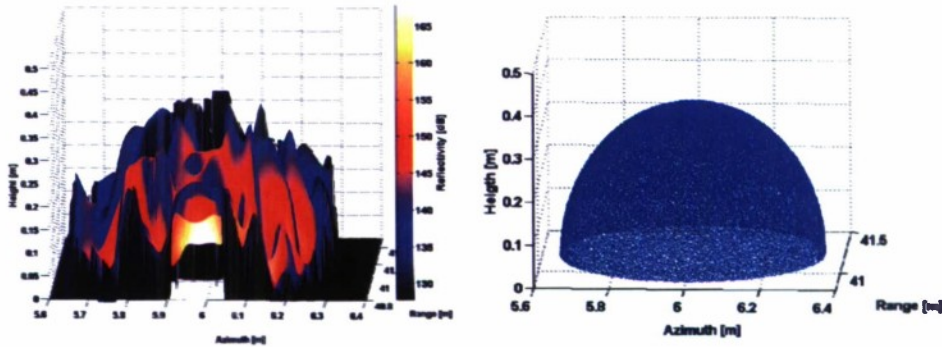


Figure 3.9 3-D view of reflectivity (left) and, for comparison, the 3-D target (right).



We observe in Figure 3.9 that the height increases towards the centre of the sphere. The shape of the sphere is quite well reconstructed. Nevertheless, we do not fully recover the shape of the sphere. Two mechanisms are identified which may explain this:

- The scattering strength of the highlight is dominant. As a result, sidelobes may influence the phase estimate at other points of the sphere.
- There is height ambiguity in range direction, as illustrated in Figure 3.10. The first response of a spherical or cylindrical target is recorded for a wave at normal incidence. When the range increases with  $\delta r$ , signal is backscattered from two different heights and is thus recorded simultaneously on array 1. Only the path lengths to array 2 differ slightly. As a result of this range ambiguity, the time (or phase) differences to the individual scatterer positions cannot be resolved. This mechanism is illustrated in Figure 3.11. It illustrates that we only obtain an estimate of the phase difference corresponding to the average height.

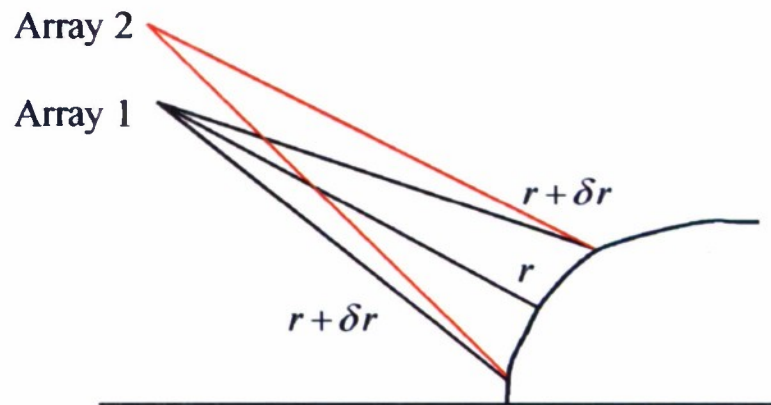


Figure 3.10 Height ambiguity with range; the first response of a spherical or cylindrical target is recorded for a wave at normal incidence. When the range increases with  $\delta r$ , signal is backscattered at two different heights and is thus recorded simultaneously on array 1. The path lengths of these two scatterer positions to array 2 differ slightly.

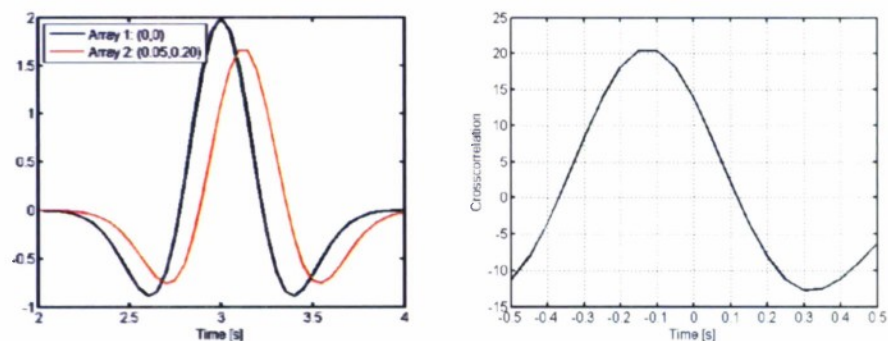


Figure 3.11 Conceptual illustration of effect of range ambiguity on recorded waveforms and on the estimated time difference. The waveform recorded on array 1 at range  $r + \delta r$  and the corresponding waveform on array 2 (left panel). The additional path lengths of the individual scatterers to array 2 are 0.05 and 0.20 s, respectively. The cross-correlation of the signals received at array 1 and 2 shows that only the average of these path length differences can be resolved (right panel).



## 4 SAS interferometry applied to DERA/GESMA rail data

### 4.1 Introduction to the DERA/GESMA rail datasets

In 1999, rail based experiments were conducted by DERA (Defence Evaluation and Research Agency - UK) and GESMA (Groupe d'Études Sous-Marines de l'Atlantique - FR) in the bay of Brest at Lanvéoc (FR). The goal of this campaign was to gather data in a semi-controlled environment to further improve different types of algorithms such as SAS and InSAS.

The sonar system used is mounted on a rail (see Figure 4.1) and is composed of two receiving arrays of 32 elements each, vertically separated by 21.7 cm. A source is placed under the two receiving arrays, that emits LFM pulses in the frequency band of 120 kHz to 180 kHz. Detailed parameters of the acquisition are presented in Table 4.1.

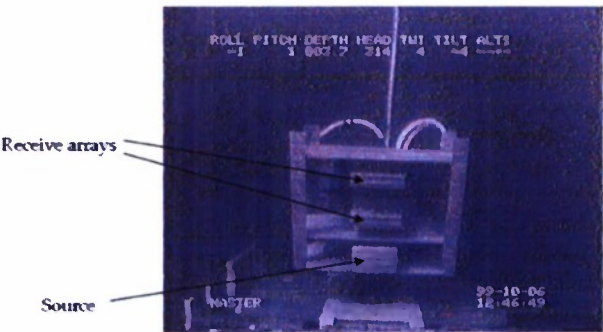


Figure 4.1 Sonar system mounted on a rail: the system is composed of two receive arrays and a source and moves along the rail axis.

Table 4.1 Acquisition parameters.

Parameters of the system	Value
Centre frequency [kHz]	150
Sampling frequency [kHz]	560
Bandwidth [kHz]	60
Pulse length [s]	0.004
Pulse repetition time [s]	3.34
Platform speed [m/s]	0.01
Space between elements [m]	0.00834
Displacement between pings [m]	0.0334
Total number of elements	64
Number of elements per array	32
Vertical array separation [m]	0.217
Total number of pings	320
Sound velocity [m/s]	1495
Number of samples	16384

On the test field across the test rail, several mine-like objects were placed on the sea floor at four different ranges. A sketch and corresponding sidescan survey of the test area are found in Figure 4.2 and Figure 4.3, respectively.

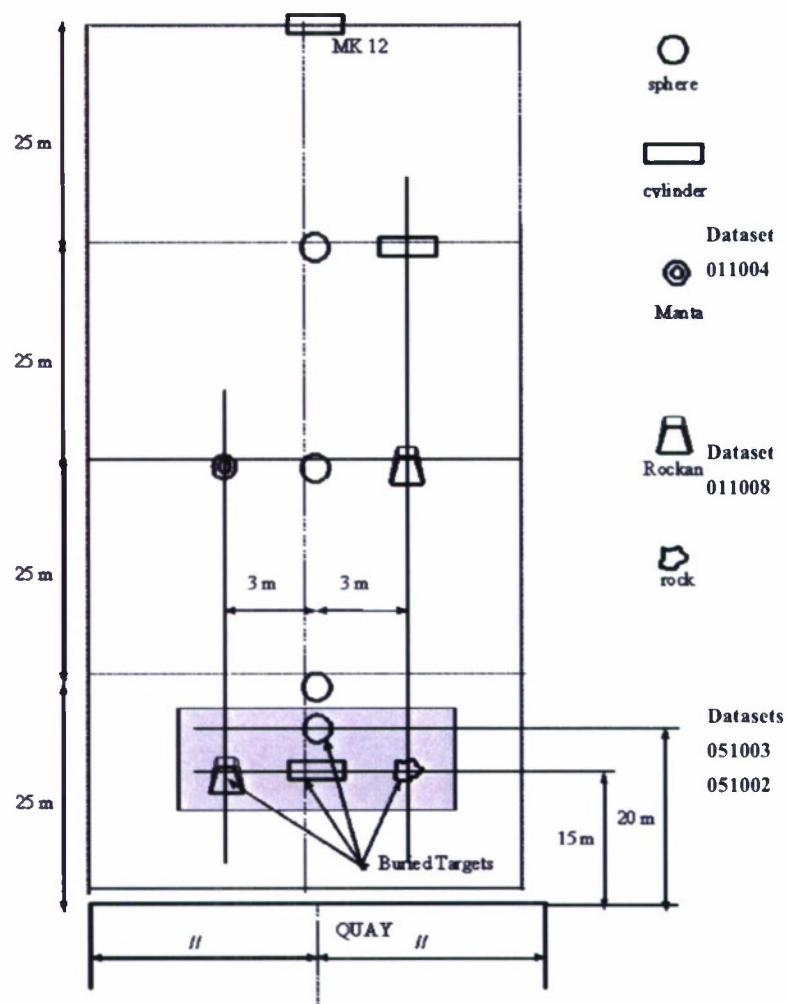


Figure 4.2 Rail experiments (GESMA-DERA, 1999): The sonar system is mounted along the quay and faces the measurement field. The target field is divided in 25 m zones where different targets are deployed. At 15 m, different targets are buried: a sphere, and two mine-like targets: a rockan and a manta. At 20 m a mine-like sphere is also buried. At 25 m a mine-like sphere is placed on the seabed. Three mine-like targets are placed at 50 m range: a manta, a rockan and a sphere. At 75 m two more mine-like targets: a cylinder and a sphere and at 100 m a mk12 mine-like cylinder. The corresponding datasets are mentioned at the right side of the field.

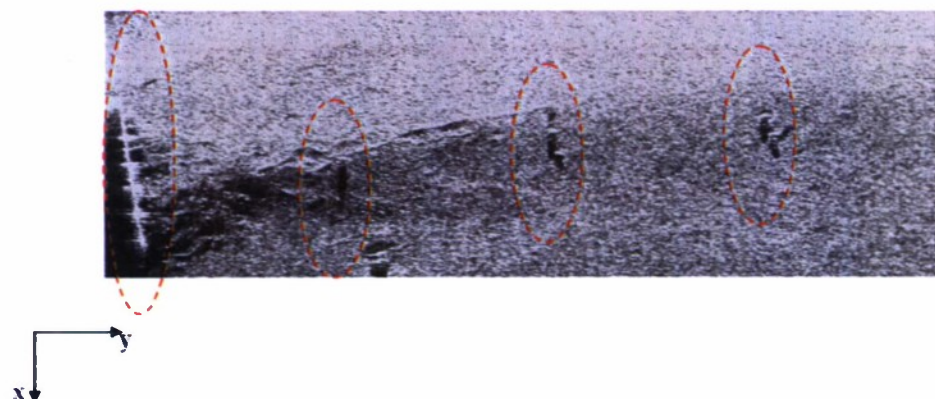


Figure 4.3 Side scan survey of the test area: on the left we can distinguish the rail where the sonar was. On the right side of the rail, along the y-axis, the targets at three different ranges (25, 50, 75 m) can be distinguished.

Table 4.2 Experiment descriptions.

Experiment Number	Description
051002	Spherical mine-like target at 25 m
051003	
011008	Manta, spherical and rockan mine-like targets at 50 m
011004	Spherical and cylindrical mine-like targets at 75 m

The different tested targets are mine-like objects.

Table 4.3 Targets.

Target	Description
Sphere	1 m diameter
Cylinder	55 cm diameter and 90 cm long

Despite the parameters given in Table 4.1, a few parameters are still unknown and the most important ones are the platform height above the seafloor, which is one of the required parameter for InSAS ( $h$  in Equation 2.5) and the range vector corresponding to the data acquisition (i.e. a time reference). These parameters had to be deduced and estimated from the acoustical data itself, because they were not documented. In order to determine the range bracket, a SAS migration for various range vectors was performed trying to optimise the contrast on the spherical target. An estimate of the height of the platform is inferred from the shadow length. The parameters for experiments 011004 and 051003 are summarised in Table 4.4 and Table 4.5, respectively.

4.2 Description of processing sequences

4.2.1 Quality control

Before any SAS processing is applied to the raw data, it has to undergo a quality control sequence in several steps in order to optimize the final SAS picture. For further reference, channels 1 to 32 correspond to the lower array (later referred to as array 1) and channels 33 to 64 correspond to the upper array (later referred to as array 2).

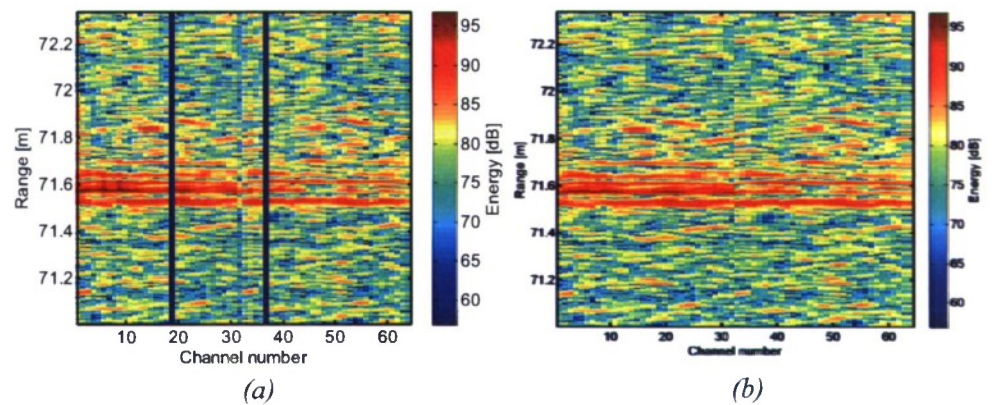


Figure 4.4 Ping 160. Raw data (a) and the same data after amplitude equalization/interpolation (b).

A limited range bracket from one ping of the 011004 dataset is presented in Figure 4.4. The left panel (a), shows that defective channels occur, containing invalid data. This may be due to bad connections and short-circuits in the array electronics, causing duff channels (blue columns containing zeroes) and –less visible– identical

neighbouring channels, respectively. These defective channels are restored by interpolation of the neighbouring channels, resulting in Figure 4.4 (b).

Additional to channel restoration, amplitude equalisation is performed. Channel amplitudes may vary slightly due to differences in element sensitivity, gain factors and other causes, as illustrated in Figure 4.5.

In order to correct these small effects, amplitude equalization is performed on each ping file: for each ping file, the total energy  $E_i$  along a channel  $i$  is computed:

$$E_i = \sum_{l=1}^N e_i^2(l), \text{ where } N \text{ is the number of samples. Then each trace } i \text{ is normalized}$$

by  $\sqrt{\frac{\bar{E}}{E_i}}$ , with  $\bar{E}$  the average of  $E_i$  of all traces.

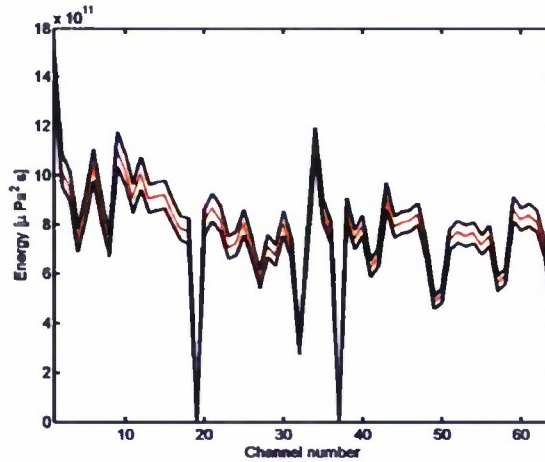


Figure 4.5 Average energy per channel, in red and standard deviation in black. This figure is an average across all pings for dataset 011004.

#### 4.2.2 Synthetic aperture formation

In order to allow coherent SAS migration, an equivalent array of midpoints is used instead of the physical receive element positions. These monostatic midpoints are located in the middle between each element and the position of the acoustic centre of the source (see Figure 4.6). Hence the effective array length is only half the physical array length.



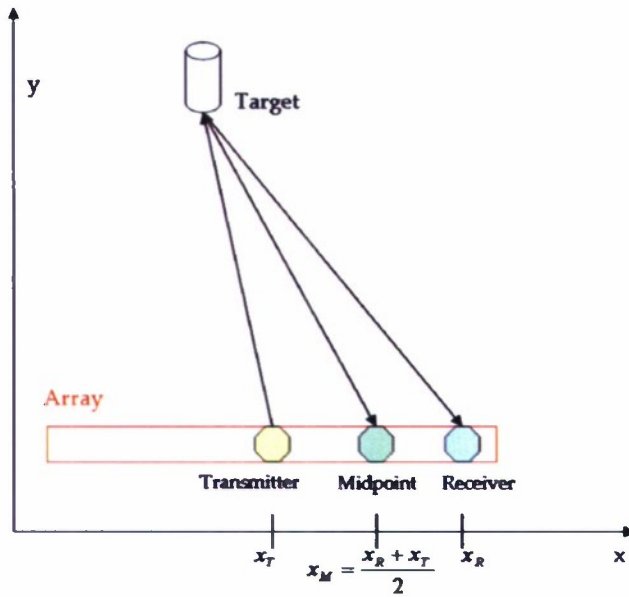


Figure 4.6 Phase centre approximation: each transmitter-receiver pair is assumed to be a monostatic equivalent located midway between the two.

The integration of successive pings is then done for common midpoints, i.e. midpoints of successive pings that are at the same location (Figure 4.7).

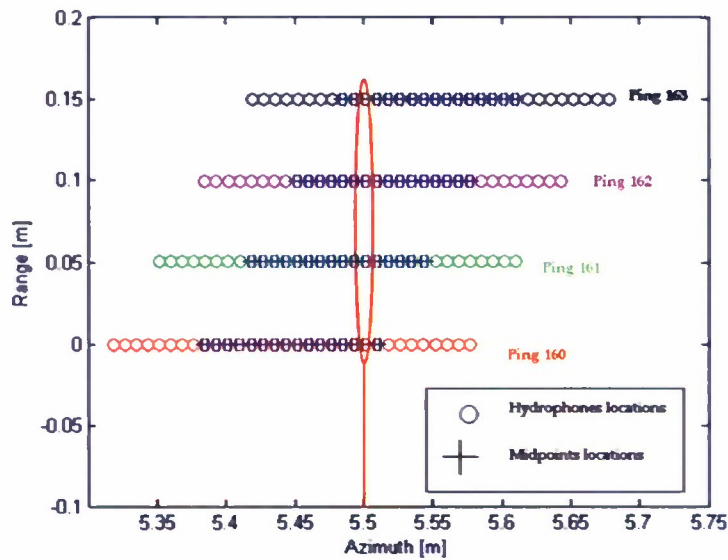


Figure 4.7 Four consecutive pings (160 to 163): for clarity, the arrays are shifted in range in this figure. The circles represent the actual element locations and the pluses (+) are the corresponding midpoint locations. The common midpoints, i.e. with the same position, are circled in red for one azimuth position. The signals from these four overlapping midpoints are summed.

In order to check if overlapping midpoints are indeed in phase, it is possible to check visually if the corresponding traces for one position are in phase or not.

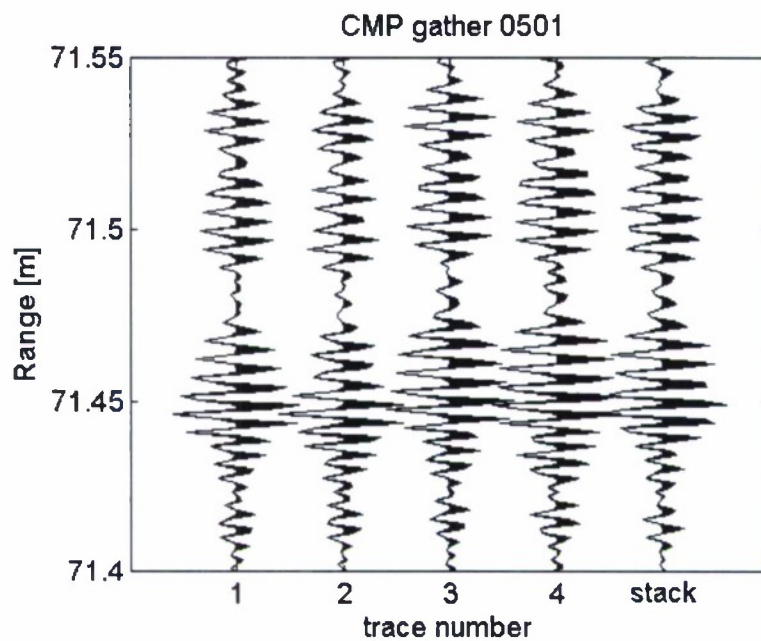


Figure 4.8 Common midpoints stacks zoomed in. The first four curves correspond to the response on the following midpoints: 1) ping 147, element 31, 2) ping 148, element 23, 3) ping 149, element 15, 4) ping 150, element 7. The right-curve is the normalised summation of the four common midpoints. In theory the five curves should be exactly aligned in range and with the same amplitude, which is not the case; there are indeed some (small) shifts, and as a result the summed curve has a lower amplitude.

The misalignment visible in Figure 4.8 is caused by an offset in the position of the receive arrays themselves. Despite being on a rail, it was found that the sonar system is not perfectly aligned with the rail axis, leading to a crabbing angle (Figure 4.9). Other motions (especially *sway* –sideways displacement– and *yaw* –rotation around the vertical axis–) are negligible due to the nature of the platform. This position error must be corrected to allow a coherent summation of the different traces.

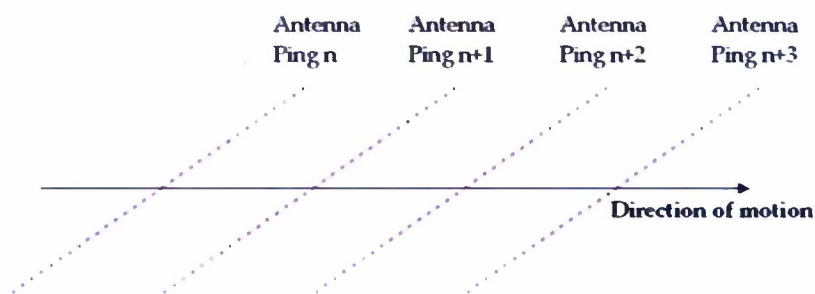


Figure 4.9 Illustration of magnified crabbing angle: constant angle between the axis of the antenna and the direction of motion.

#### 4.2.3 Motion compensation

A rail is an extremely stable platform in terms of motion, especially compared to a ship. Still, for SAS imaging, a motion error exceeding  $\lambda/10$ , where  $\lambda$  corresponds in this case to the highest frequency transmitted, could cause defocusing of the output image. This corresponds to an error greater than 0.8 mm in our case, which is very small. Moreover, SAS interferometry is even more sensitive to motion errors than SAS imaging. The rail can therefore not be considered as a linear track and its accurate motion has to be derived from the acoustic signals themselves. This approach is generally referred to as autofocus. As mentioned previously, a crabbing angle was found in the system, which has to be corrected. All other motions (especially yaw and sway, which are most disturbing for SAS imagery) were found negligible.

A well known and used technique for this purpose is the displaced phase centers (DPC) method [17], [20]. This method uses the previously mentioned phase centers and is based on correlating two consecutive pings: A matrix of absolute cross-correlation values can be created for two consecutive pings, consisting of all possible combinations of array elements. The highest values in the matrix indicate the displacement between those pings, expressed in number of array elements. The example in Figure 4.10 shows a displacement of 8 elements along the array axis (*along track*).

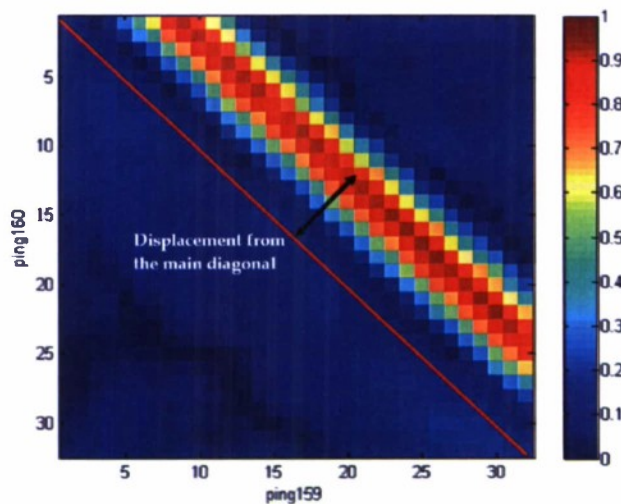


Figure 4.10 Displaced phase centre method for motion estimation: on the X-axis there is ping  $n$  and on the Y-axis there is ping  $(n+1)$ . The represented values correspond to the correlation coefficients.

The current DPCA algorithm cannot distinguish between a fixed crabbing angle and constant sway as illustrated in Figure 4.11. It illustrates the correspondence between an angle corresponding to a constant sway drift and a constant crabbing angle:

$\theta_{SWAY} = \theta_{CRABBING}$ . If this is interpreted as a sideways displacement, this will result in increasing lateral displacements along the path, as shown in Figure 4.12.

For our purpose, i.e. estimating the crabbing angle, the sway displacement had to be derived first before being converted to a crabbing value. First, the along track displacement is estimated from the displacement between the main diagonal and the diagonal with the highest values (see Figure 4.10). This gives the corresponding phase centers for two consecutive pings. The time lag of the cross-correlation peak then yields

the displacement in the range direction (*cross-track*). The average value of all overlapping elements yields the sway estimate.

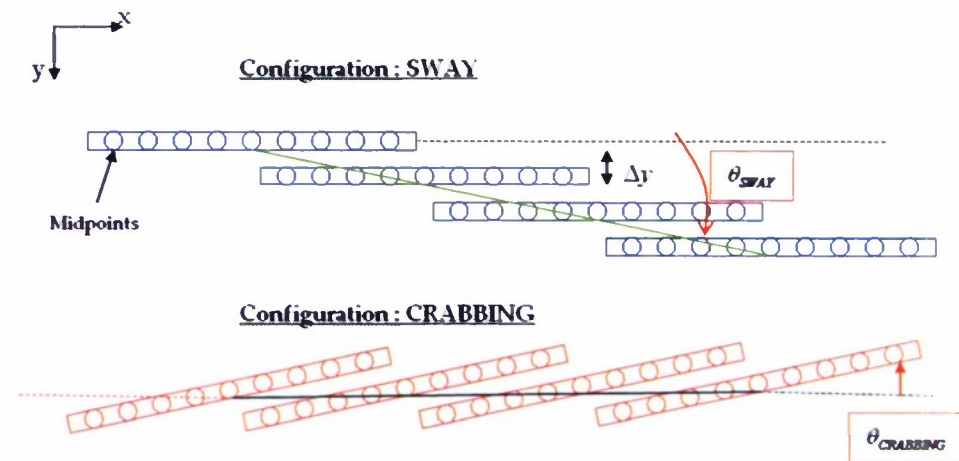


Figure 4.11 Top figure is the configuration of a sway motion: the DPC algorithm assumes that we have this situation and between each ping it computes the sway  $\Delta y$ . But in case of rail measurements it is not possible to have such a configuration. However, by rotating the top figure, we obtain the bottom one that represents the crabbing angle configuration.

The DPC algorithm is thus applied to the total considered dataset and the trajectory of each channel is estimated (in blue for only one element in Figure 4.12). The green line is the linear regression corresponding to the sway displacement and, as just explained, this gives us a direct estimate of the crabbing angle.

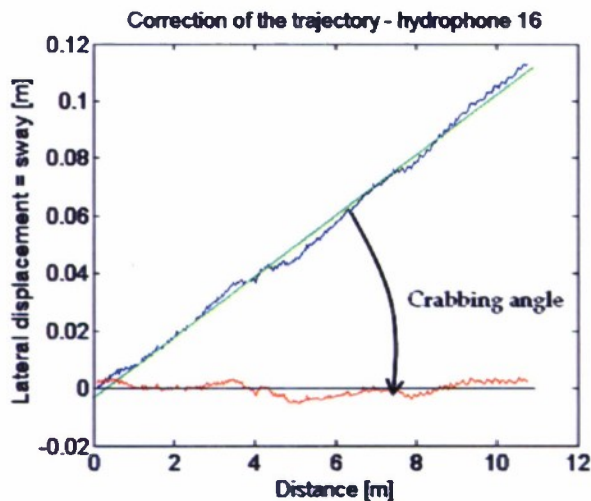


Figure 4.12 Estimation of the crabbing angle: only element 16 is represented so that the drawing is clearer. In blue the lateral displacement estimated with the DPC algorithm and in green the corresponding linear regression. In red, the projection of the blue curve on the along track, i.e. the real movement of the sonar and the black line is the rail axis.

Once the crabbing angle has been estimated (0.7 degrees for this dataset), the coordinates of the phase centres can be derived: for each ping, the array is tilted with the crabbing angle as shown in Figure 4.13 and the derived calculated midpoints coordinates will then be used for the motion compensation.



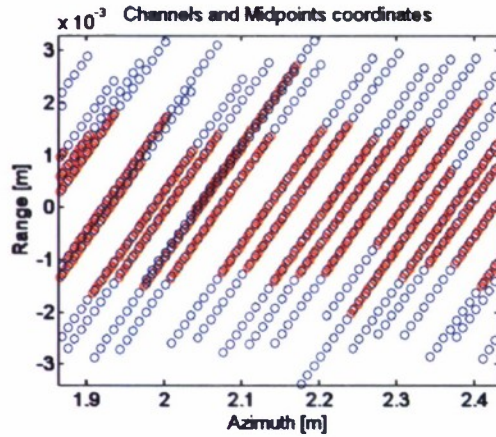


Figure 4.13 Tilted array: in blue, the calculated element positions and in red the corresponding midpoint positions. Note that scales in x- and y-direction are very different.

Using the derived positions, their range offsets are used to calculate time shifts which are then applied to the corresponding element signals. The result of this time shift will be that all motion corrected midpoints lie along the same line. Once this motion correction has been done, we can display the common midpoint gathers to see the improvement as compared with Figure 4.8:

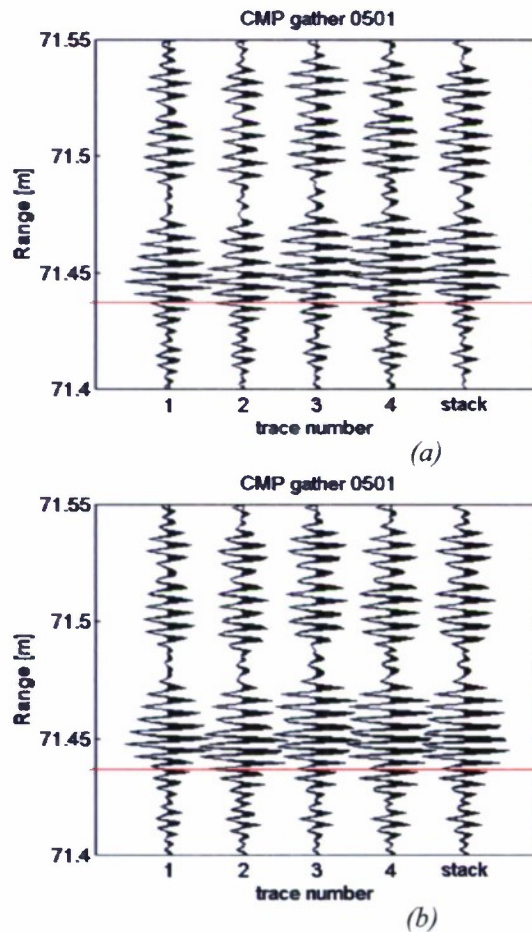


Figure 4.14 Common midpoints gather. (a) is without motion compensation, (b) is with motion compensation. We can notice that the small phase shift that was observed without motion compensation is now much smaller: on (b) the four left-hand curves are in phase and the stack curve has about the same amplitude as the four others.

The small phase shift that appeared in Figure 4.8 is now much smaller. As for the amplitude of the fifth curve, it now equals the amplitude of the first four curves.

It should be noted here that the rail configuration (i.e. assuming the sway was negligible) allowed us to derive the crabbing angle. On a more conventional platform (ship, submarine, AUV ...) the DPCA algorithm needs to be generalized (including subsequent midpoint/phase centre positions) to derive the crabbing angle and sway simultaneously.

#### 4.3 Results on DERA/GESMA rail data set 011004<sup>3</sup> (75 m range)

These data image an area with both a sphere and a cylinder at a range of approximately 75 m. Figure 4.15 shows the SAS image constructed from the data acquired by array 1.

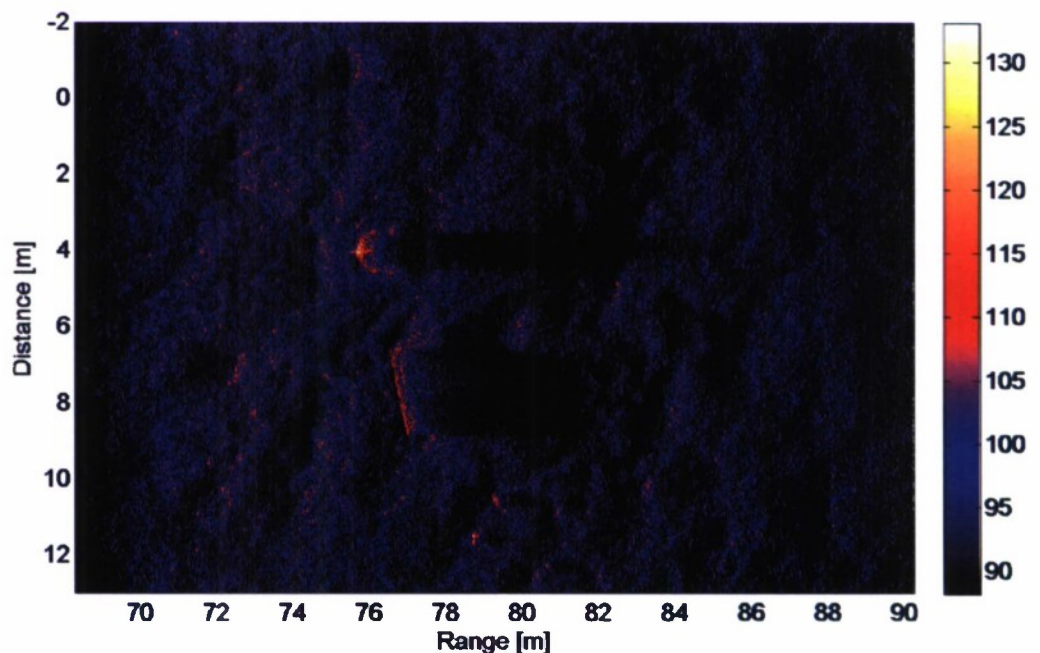


Figure 4.15 SAS image for DERA/GESMA rail data 011004, array 1.

The acquisition parameters are listed in Table 4.4. Information on the origin time of the data and the height of the platform was not available. In order to determine the range bracket, we repeated the Stolt migration for various target ranges, optimising the contrast of the spherical target. An estimate of the platform height is inferred from the shadow length. This estimate is further tuned to locate the seafloor at  $z = 0$  m depth.

<sup>3</sup> Processing: Software id = 'DERA\_GESMA\_raildata; 011004.  
Interferometry: Software id = '011004\_20080128'.

Table 4.4    Acquisition parameters for DERA/GESMA rail data 011004.

Pulse centre frequency $f_c$	150 kHz
Pulse bandwidth $b$	60 kHz
Pulse type	Linear frequency modulated pulse (LFM)
Pulse duration	4.0 ms
Length of synthetic aperture	10.7 m
Number of pings	320
Number of elements/ping	64 (32 in each array)
Separation of elements	0.00834 m
Displacement between pings	0.0334 m
Platform height relative to seafloor at target	Estimated 7.5 m ( $\pm$ 0.5 m)
Platform y-distance to targets	Approximately 75 m ( $\pm$ 0.2 m)
Number of arrays	2
Baseline vector <b>B</b> before tilting	(0, 0, 0.217) m
Baseline tilt angle	6 degrees
Origin of range vector $r_0$	Estimated 68.30 m ( $\pm$ 0.2 m)

In order to assess the success of the geometry-based co-registration, we focus on a part of the cylinder. Figure 4.16 shows that the geometrical displacement between the master and co-registered slave image is small, and thus indicates the success of the geometry-based co-registration.

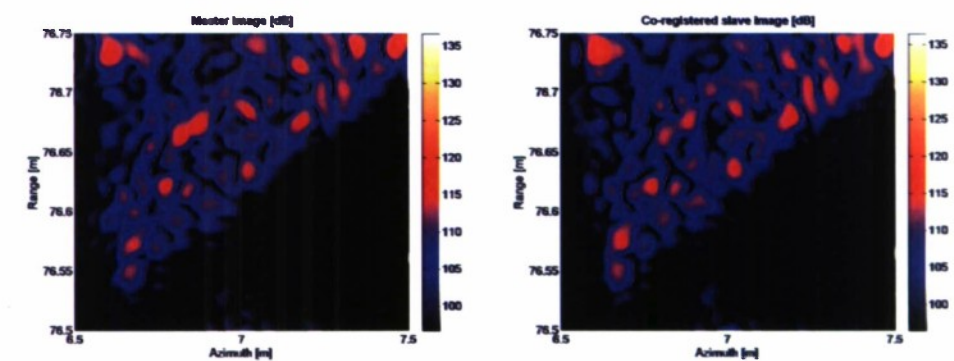


Figure 4.16    Detail of the SAS image of the cylinder illustrated in Figure 4.15, as used for interferometry. Shown are the master image obtained with array 1 on the left and the co-registered (slave) image from array 2 on the right.

As suggested by Figure 4.16, the co-registered master and slave images are highly correlated. This is confirmed by the correlation map (Figure 4.17). A correlation value equal to one indicates that the master and slave images are perfectly correlated. Low correlation values are observed, as expected, in the shadow regions (e.g. behind the sphere). Multipath propagation is another factor causing data to decorrelate. The correlation map is an important measure for quality control. If data are poorly correlated, phase estimates are likely to be uncertain. Then, the height estimates become unreliable.



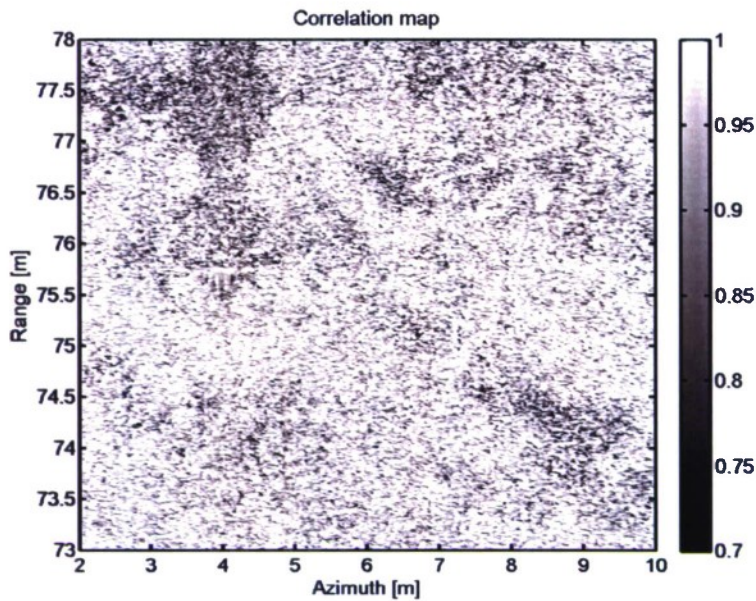


Figure 4.17 Correlation map, indicating local correlation coefficients between the master image and the co-registered slave image. High correlation is required to achieve good height estimates.

Figure 4.18 shows the interferometric height estimates. Both the sphere and the cylinder can be easily recognised. Height values with a reflectivity of  $-45$  dB relative to the maximum reflectivity have been set to zero.

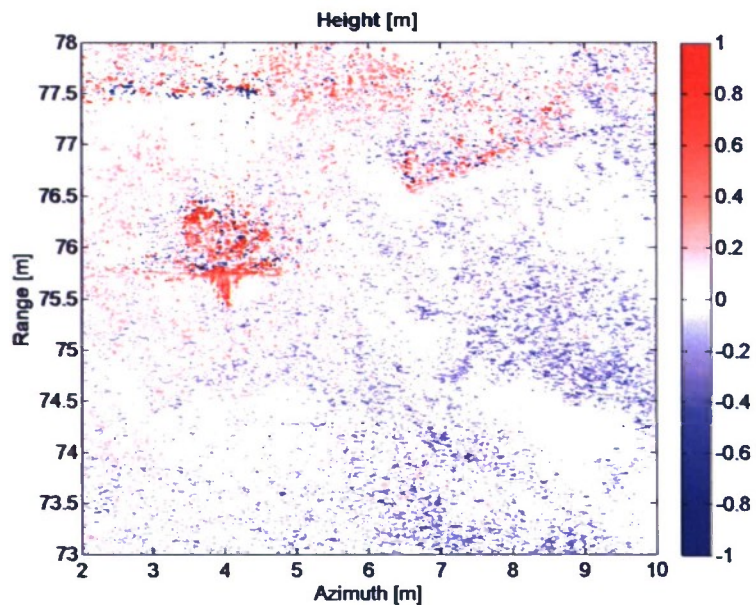


Figure 4.18 Height estimate derived from the interferogram, showing both the sphere and the cylinder.

Figure 4.19 and Figure 4.20 focus on the sphere and the cylinder and show 2D and 3D views of reflectivity. The image of the sphere has two highlights. The first highlight corresponds to the direct path, whereas the second highlight is attributed to the seabed multipath. The travel time of this multipath corresponds to an imaginary target located below the seabed. This imaginary target is a mirror image of the sphere. The 3D reflectivity map shows that interferometry indeed locates the multipath highlight below the seabed, and is therefore indicative for the resolution of the height estimates.



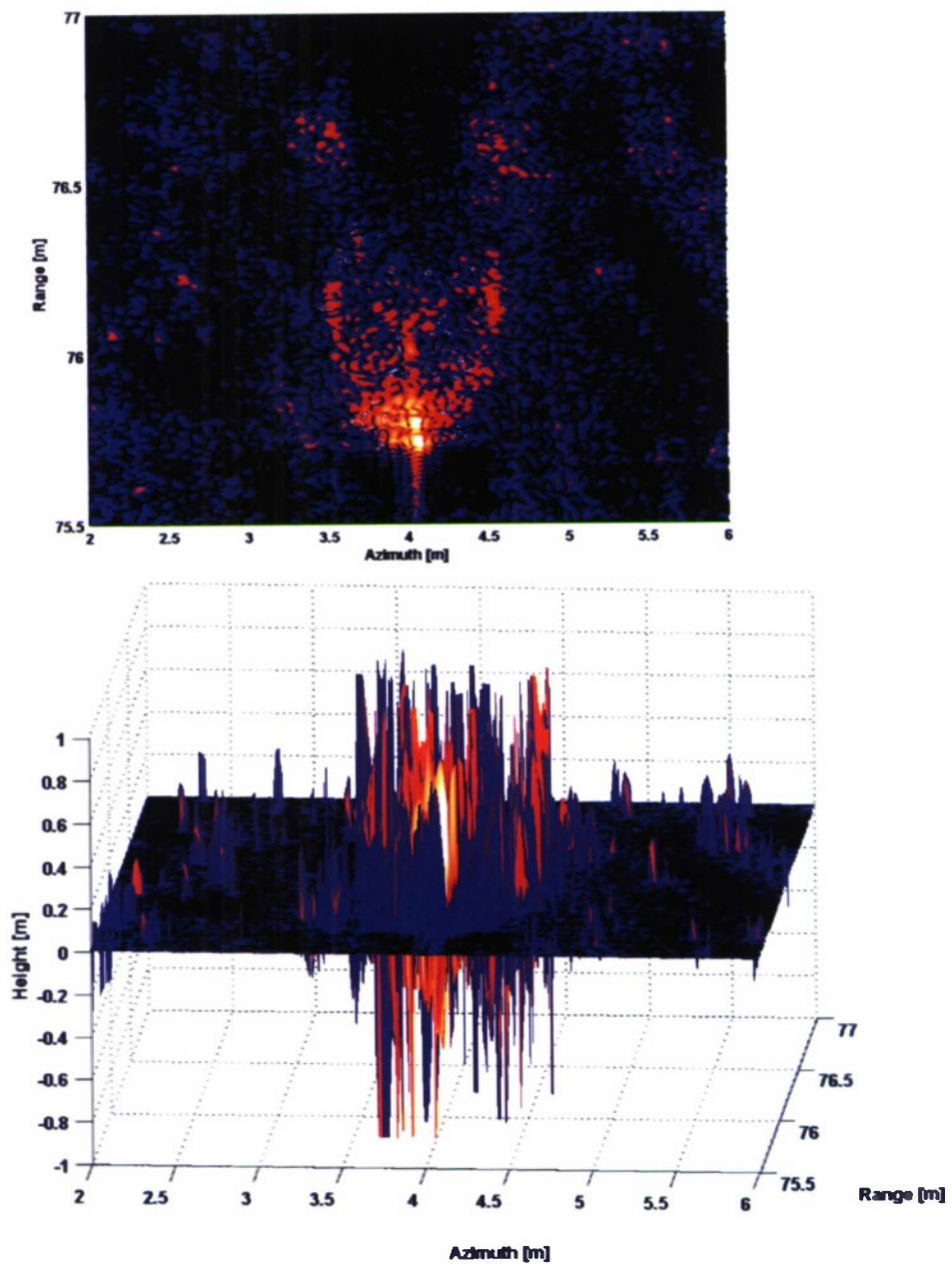


Figure 4.19 2D (top) and 3D (bottom) reflectivity images of the sphere.

In general, multipath propagation is a problem for interferometry. Reliable height estimates cannot be obtained when a pixel has a direct and a multipath scattering contribution of comparable strength. We expect that the noise in the height estimates for both the sphere and the cylinder is at least partly caused by multipath. Multipath propagation is especially relevant at low grazing angles.

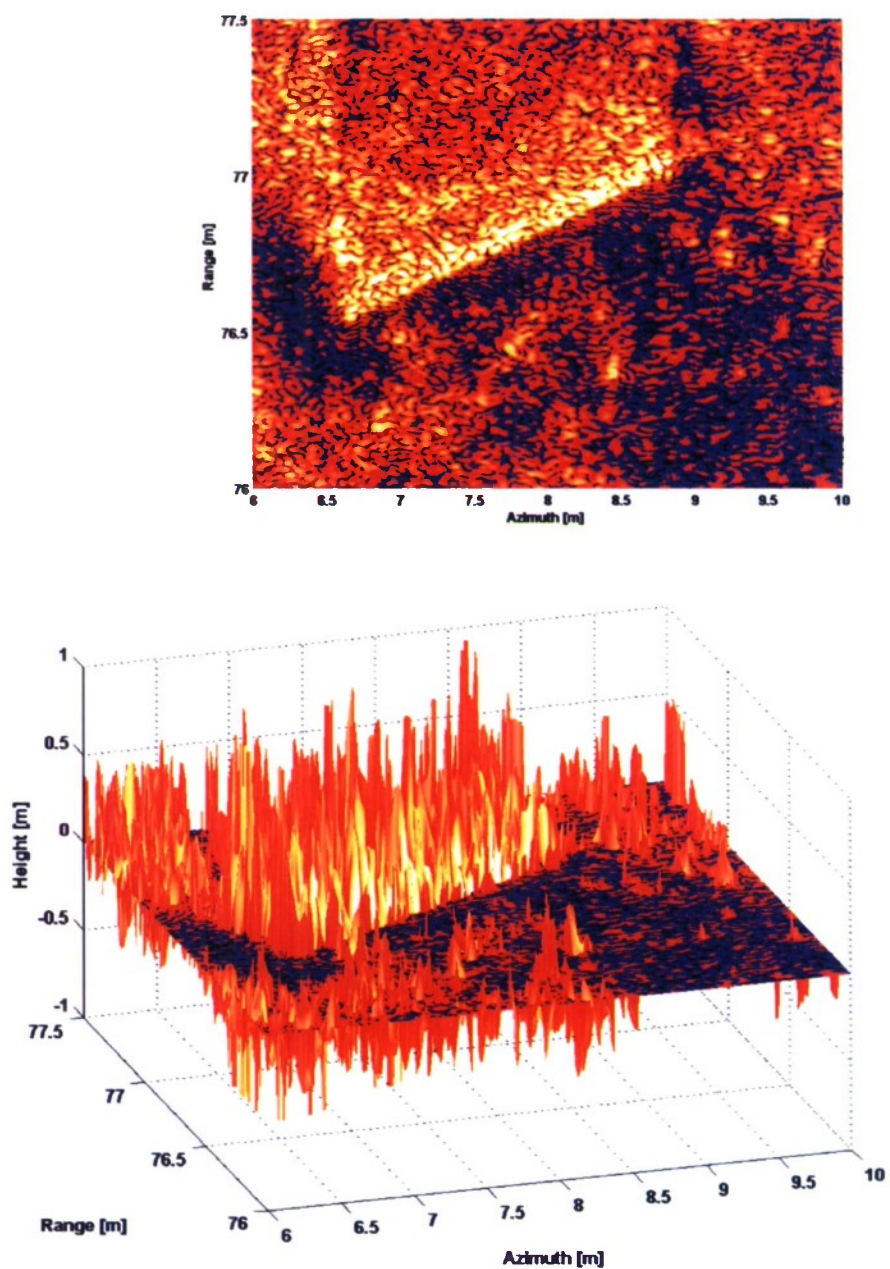


Figure 4.20 2D (top) and 3D (bottom) reflectivity images of the cylinder.

4.4 DERA/GESMA rail data set 051003<sup>4</sup> (25 m range)

This data set images an area with a target at a range of approximately 25 m. The target is a sphere with a diameter of approximately 1.0 m. As a result of the short range in comparison with the 011004 data set, the grazing angle is larger. We expect therefore that multipath will be less significant. Figure 4.21 shows the SAS image from array 1.

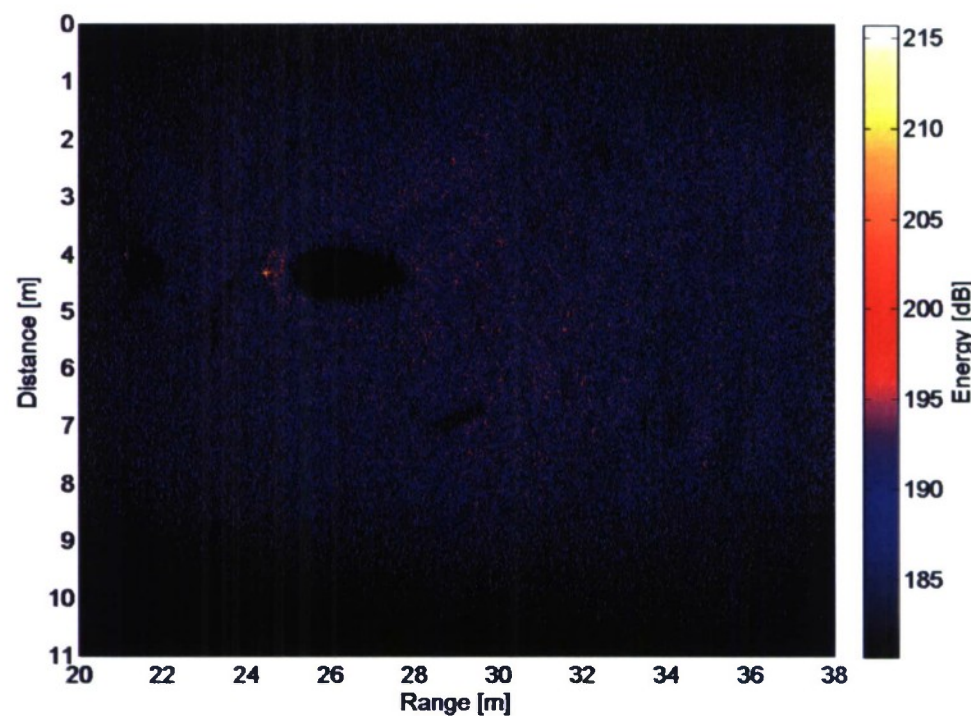


Figure 4.21 SAS image from DERA/GESMA rail data 051003.

The acquisition parameters are listed in Table 4.5. Again, the range is estimated by optimizing the contrast in the image. The height of the platform is obtained using the shadow and fine-tuned to locate the background at  $z = 0$ .

Table 4.5 Acquisition parameters for DERA/GESMA rail data 051003.

Pulse centre frequency $f_c$	150 kHz
Pulse bandwidth $b$	60 kHz
Pulse type	Linear frequency modulated pulse (LFM)
Pulse duration	4.0 ms
Length of synthetic aperture	10.7 m
Number of pings	320
Number of elements/ping	64 (32 in each array)
Separation of elements	0.00834 m
Displacement between pings	0.0334 m
Platform height relative to seafloor at target	Estimated 9.2 m ( $\pm 0.5$ m)
Platform y-distance to targets	Approximately 25 m ( $\pm 0.2$ m)

<sup>4</sup> Processing: Software id = 'DERA\_GESMA\_raildata; 051003'.  
Interferometry: Software id = '051003\_20080128'.



Table 4.5 Acquisition parameters for DERA/GESMA rail data 051003 (continued).

Number of arrays	2
Baseline vector <b>B</b> before tilting	(0, 0, 0.217) m
Baseline tilt angle	14 degrees
Origin of range vector $r_0$	Estimated 13.50 m ( $\pm$ 0.2 m)

Details of the background imaged in both the master and slave image show that these are highly correlated (Figure 4.22), and this is confirmed by the correlation map (Figure 4.23). The data are highly correlated except on the target itself.

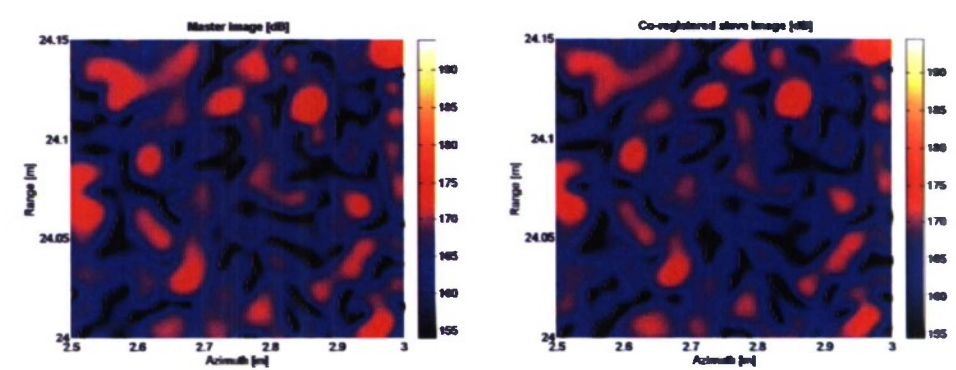


Figure 4.22 Detail of the background in the SAS image illustrated in Figure 4.21. Shown are the master image from array 1 and the co-registered image from array 2.

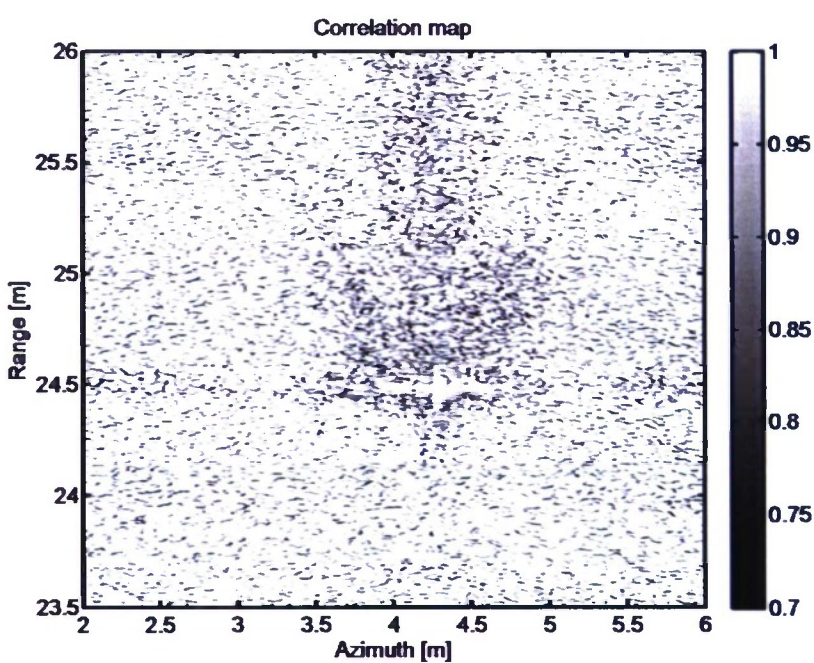


Figure 4.23 Correlation map, indicating local correlation coefficients between the master image and the co-registered slave image of the sphere and a patch of surrounding seafloor. High correlation is required to achieve good height estimates.

The interferometric height estimates (Figure 4.24 and Figure 4.25) show that the background is very flat and well resolved. On the other hand, the height of the target is not well resolved. This is presumably related to phase unwrapping problems. These unwrapping errors may be caused by the discontinuity in the height at the edge of



the sphere. Assuming that the subsidence of the target can be neglected, the height of the normal incidence target highlight is located approximately 0.6 m above the seafloor, about 10 cm higher than the sphere midpoint due to the incidence angle. The corresponding path differences to array 1 and 2 are of similar order of magnitude as the wavelength (0.01 m). Therefore, we expect that the negative height values are phase unwrapping artefacts. Another possibility is multipath propagation as discussed in the previous section.

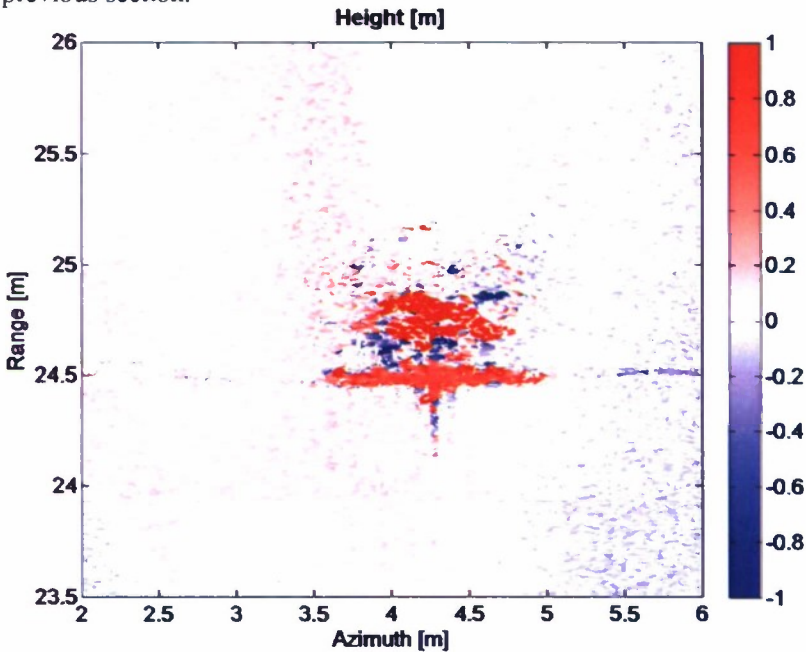


Figure 4.24 Height estimate derived from the interferogram (after phase unwrapping).

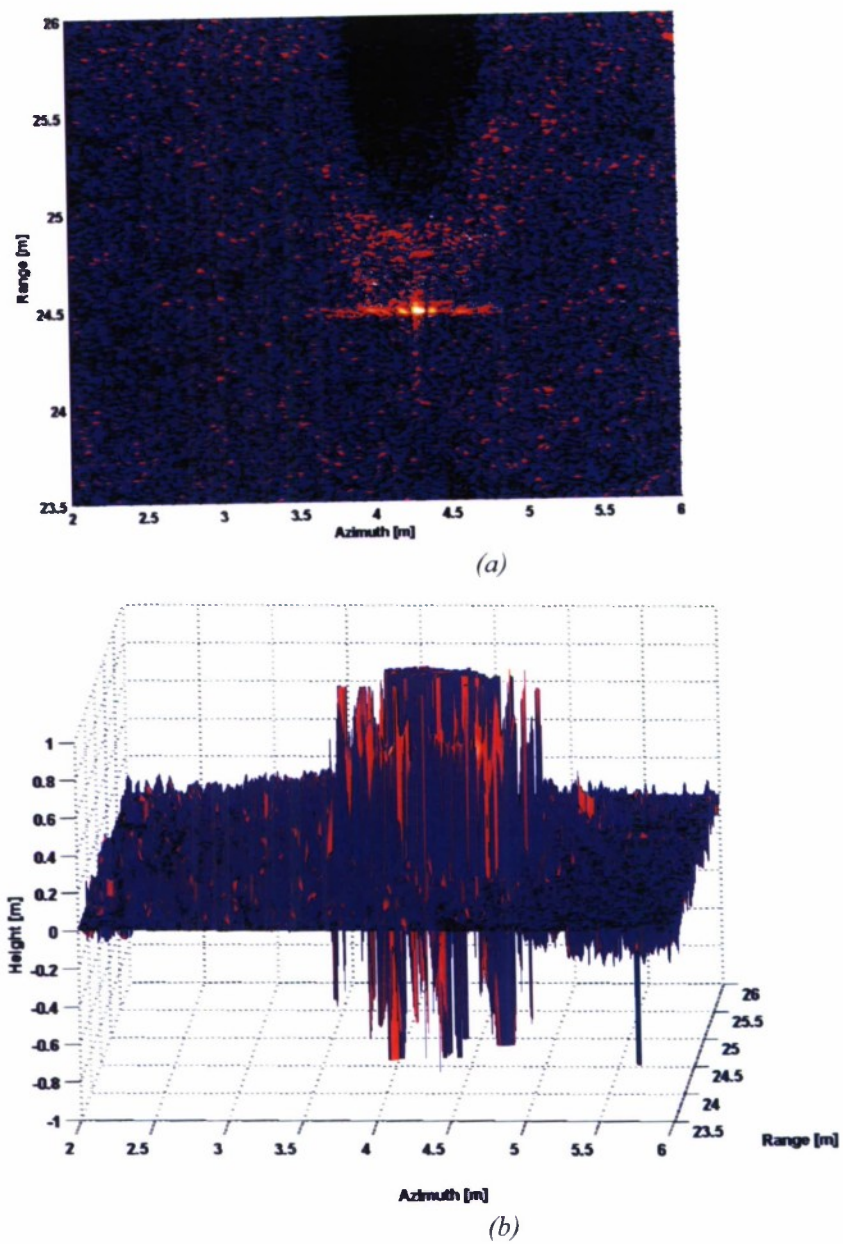


Figure 4.25 2D (a) and 3D (b) reflectivity images of the sphere.

## 5 Conclusions and outlook

The preceeding chapters have described the status of interferometric SAS processing at TNO. The current implementation uses SAS processing as an initial step. Then, interferometric processing is applied to the SAS images to infer the height. Experiments with both simulated and measured data provided promising and interesting results. These gave insight into the prospects – such as valid height values corresponding to the targets and for the bathymetry – but also helped us to identify limitations of SAS interferometry.

The most important limitation is the variability of the height estimates in both the simulated and measured data. This addresses a fundamental issue, i.e. that the SAS processing needs to be *phase-preserving*. In the presence of strong scatterers, imaging artefacts (*sidelobes*) in the vicinity of the scatterer cause a considerable amount of noise in the phase information. Furthermore, interferometry is very sensitive to *platform motion* errors, and height estimates are also unreliable in the case of *multipath propagation* (height ambiguity with range).

Further development of SAS interferometry should be aimed at improving the reliability of the phase information. The following aspects are aimed at resolving the above-mentioned bottlenecks:

- We need to consider the interferometric processing. Instead of starting with the SAS imaging, which aims at optimising the contrast in the images, *specific interferometric imaging* needs to be considered. This processing should include a compensation for highlights to suppress sidelobes.
- In addition, the higher sensitivity to motion errors requires to reconsider the optimum integration angle (or synthetic aperture length). A shorter aperture decreases the sensitivity to motion errors. This should be balanced with the loss in azimuth resolution. The results obtained in different sub-apertures can be combined, to improve the S/N ratio of the phase estimates.
- It has been shown that the accuracy of the instantaneous phase estimate decreases with increasing bandwidth (Figure 2.4). As a consequence, there is a tradeoff between the accuracy of the interferometric height estimate and the range resolution that can be achieved, which advocates processing at reduced bandwidth. In general, the interferometric resolution will be significantly lower than in the reflectivity images.
- Finally, a more sophisticated method for phase unwrapping has to be implemented. Phase unwrapping errors lead to erroneous height estimates. Special attention is required to resolve these ambiguities when there are discontinuities in height (e.g. when a spherical object is located on the seabed).

A remaining challenge is to obtain reliable phase information in the presence of multipath propagation, which is also referred to as overlay.

The developed algorithms will eventually be applied to low-frequency buried-mine data. It is expected that distinguishing bottom echoes from echoes from below will improve detection performance. An experiment on objects buried in mud will most likely take place in 2009. Adjustments and modifications to the software will no doubt be necessary, but the interferometric toolbox is now available and operational.

## 6 References

- [1] Rosen, P.A., Hensley, S. Joughin, I.R., Li, F.K., Madsen, S.N., Rodriguez, E., and Goldstein, R.M., "*Synthetic aperture radar interferometry*", Proceedings of the IEEE, 88(3), 333-382, 2000.
- [2] Bamler, R., and Hartl, P., "*Synthetic aperture radar interferometry*", Inverse Problems 14, R1-R54, 1998.
- [3] Griffiths, H.D., et al., "*Interferometric synthetic aperture sonar for high-resolution 3-D mapping of the seabed*", IEE Proc. Radar Sonar Navigation 144(2): 96-103, 1997.
- [4] Sæbø, T.O., Hansen, R.E., Callow, H.J., "*Height estimation on wideband synthetic aperture sonar: experimental results from InSAS-2000*", Oceans 2005.
- [5] Bonifant, W.W., "*Interferometric synthetic aperture sonar processing*", Msc. Thesis, Georgia Institute of Technology, 1999.
- [6] Barclay, J.P., "*Interferometric synthetic aperture sonar design and performance*", PhD Thesis, University of Canterbury, 2006.
- [7] Hansen, R.E., Sæbø, T.O., Callow, H.J. and Hagen, P.E., "*Synthetic aperture sonar processing for the HUGIN AUV*", Oceans 2005.
- [8] Hagen, P.E., Hansen, R.E., and Langli, B., "*Interferometric synthetic aperture sonar for the HUGIN 1000-MR AUV*", UDT Pacific 2006.
- [9] Vernier, A., "*Interferometric synthetic aperture sonar for the detection of buried objects*" Msc. Thesis, ENSIETA, 2007.
- [10] Barnes, A. E., "*A tutorial on complex trace analysis*", Geophysics, **72**, pp. W33-W43, 2007.
- [11] Sheriff, R.E., "*Encyclopedic dictionary of applied geophysics, 4<sup>th</sup> ed*", Society for Exploration Geophysicists, 2002.
- [12] Goldstein, R.M., Zebker, H.A., and Werner, C.L., "*Satellite radar interferometry: two-dimensional phase unwrapping*", Radio Science, **23**, 713-720, 1988.
- [13] Ghiglia, D.C., and Pritt, M.D., "*Two-dimensional phase unwrapping: Theory, Algorithms, and Software*", Wiley, New York, 1998.
- [14] Chen, C.W., and Zebker, H.A., "*Network approaches to two-dimensional phase unwrapping*", Journal of the Optical Society of America A, **17(3)**, 401-414, 2000.
- [15] Chen, C.W., and Zebker, H.A., "*Two-dimensional phase unwrapping with use of statistical models for cost functions in nonlinear optimization*", Journal of the Optical Society of America A, **18(2)**, 338-351, 2001.
- [16] Chen, C.W., and Zebker, H.A., "*Phase unwrapping for large SAR Interferograms: Statistical segmentation and generalized network models*", IEEE Transactions on Geoscience and Remote Sensing, **40**, 1709-1719.
- [17] Groen, J., "*Adaptive motion compensation in sonar array processing*", PhD. Thesis TU Delft, 2006.
- [18] Stolt, R.H., "*Migration by Fourier transform*", Geophysics, **43**, 23-48, 1978.

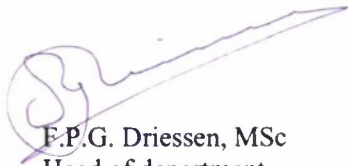


- [19] Yilmaz, O., "*Seismic data analysis, vol I*", Society for Exploration Geophysicists, 2002.
- [20] Belletini, A. and Pinto, M. A., "*Theoretical accuracy of synthetic aperture sonar micronavigation using a displaced phase-center antenna*", IEEE Journal of Oceanic Engineering, **27**, 780-789, 2002.


## 7 Signature

The Hague, October 2008

TNO Defence, Security and Safety



F.P.G. Driessen, MSc  
Head of department



Dr R. van Vossen  
Author

**ONGERUBRICEERD**  
**REPORT DOCUMENTATION PAGE**  
(MOD-NL)

1. DEFENCE REPORT NO (MOD-NL) TD2008-0067	2. RECIPIENT'S ACCESSION NO -	3. PERFORMING ORGANIZATION REPORT NO TNO-DV 2008 A176
4. PROJECT/TASK/WORK UNIT NO 015.34736	5. CONTRACT NO -	6. REPORT DATE October 2008
7. NUMBER OF PAGES 44 (excl RDP & distribution list)	8. NUMBER OF REFERENCES 20	9. TYPE OF REPORT AND DATES COVERED Final
10. TITLE AND SUBTITLE The prospects of SAS interferometry for detection and classification		
11. AUTHOR(S) Dr R. van Vossen B.A.J. Quesson Dr J.C. Sabel		
12. PERFORMING ORGANIZATION NAME(S) AND ADDRESS(ES) TNO Defence, Security and Safety, P.O. Box 96864, 2509 JG The Hague, The Netherlands Oude Waalsdorperweg 63, The Hague, The Netherlands		
13. SPONSORING AGENCY NAME(S) AND ADDRESS(ES) Royal Netherlands Army		
14. SUPPLEMENTARY NOTES The classification designation Ongerubriceerd is equivalent to Unclassified, Stg. Confidentieel is equivalent to Confidential and Stg. Geheim is equivalent to Secret.		
15. ABSTRACT (MAXIMUM 200 WORDS (1044 BYTE)) Processing for interferometric synthetic aperture sonar has been developed, and tested with both measured and simulated data. Interferometry is based on data from two vertically separated receive arrays. Subtle phase differences between the images from both arrays provide information on the relative height of objects in the observed scene. The results give confidence in the processing and provide insight into the limitations and options for improvement of the current processing suite. Eventually, the developed processing is expected to improve the detection of objects buried in the sea bottom.		
16. DESCRIPTORS Synthetic aperture sonar, interferometry, buried mines		IDENTIFIERS
17a. SECURITY CLASSIFICATION (OF REPORT) Ongerubriceerd	17b. SECURITY CLASSIFICATION (OF PAGE) Ongerubriceerd	17c. SECURITY CLASSIFICATION (OF ABSTRACT) Ongerubriceerd
18. DISTRIBUTION AVAILABILITY STATEMENT Unlimited Distribution		17d. SECURITY CLASSIFICATION (OF TITLES) Ongerubriceerd

**ONGERUBRICEERD**

## Distribution list

**The following agencies/people will receive a complete copy of the report.**

- |       |  |
|-------|--|
| 1     | DMO/SC-DR&D<br>standaard inclusief digitale versie bijgeleverd op cd-rom   |
| 2/3   | DMO/DR&D/Kennistransfer  |
| 4     | Programma-/projectbegeleider Defensie<br>LTZ1 drs. R.P.A. Dekeling   |
| 5     | DMO/DWS&B/RZS&B/Sensor- en Wapentechnologie (SWT)<br>LTZ1 B.E.A. Kerstens, MSc   |
| 6/8   | Bibliotheek KMA  |
| 9     | Programmaleider TNO Defensie en Veiligheid, dr.ir. J.C. Sabel  |
| 10/11 | TNO Defensie en Veiligheid, vestiging Den Haag,<br>Archief   |
| 12/17 | TNO Defensie en Veiligheid, vestiging Den Haag,<br>Business Unit Waarnemingssystemen,<br>dr. R. van Vossen<br>B.A.J. Quesson<br>ir. F.P.G. Driessen<br>dr.ir. G. Blacquiere<br>dr. S.P. Beerens<br>dr.ir. A.L.D. Beckers |



**The following agencies/people will receive the management summary and the distribution list of the report.**

- 4 ex. DMO/SC-DR&D
- 1 ex. DMO/ressort Zeesystemen
- 1 ex. DMO/ressort Landsystemen
- 1 ex. DMO/ressort Luchtsystemen
- 2 ex. BS/DS/DOBBP/SCOB
- 1 ex. MIVD/AAR/BMT
- 1 ex. Staf CZSK
- 1 ex. Staf CLAS
- 1 ex. Staf CLSK
- 1 ex. Staf KMar
- 1 ex. TNO Defensie en Veiligheid, Algemeen Directeur,  
ing. J.V. Elsendoorn
- 1 ex. TNO Defensie en Veiligheid, Directie  
Directeur Operaties, ir. C. Eberwijn
- 1 ex. TNO Defensie en Veiligheid, Directie  
Directeur Kennis, prof. dr. P. Werkhoven
- 1 ex. TNO Defensie en Veiligheid, Directie  
Directeur Markt, G.D. Klein Baltink
- 1 ex. TNO Defensie en Veiligheid, vestiging Den Haag,  
Manager Waarnemingssystemen (operaties), ir. B. Dunnebier PDeng
- 1 ex. TNO Defensie en Veiligheid, vestiging Den Haag,  
Manager Informatie en Operaties (operaties), ir. P. Schulein
- 1 ex. TNO Defensie en Veiligheid, vestiging Rijswijk, daarna reserve  
Manager Bescherming, Munitie en Wapens (operaties), ir. P.J.M. Elands
- 1 ex. TNO Defensie en Veiligheid, vestiging Rijswijk,  
Manager BC Bescherming (operaties), ir. R.J.A. Kersten
- 1 ex. TNO Defensie en Veiligheid, vestiging Soesterberg,  
Manager Human Factors (operaties), drs. H.J. Vink